# TECHNOLOGY DEVELOPMENT FOR EXOPLANET MISSIONS

## Technology Milestone Report

## A Photon-Counting Detector for Exoplanet Missions

**Dr. Donald Figer, PI**
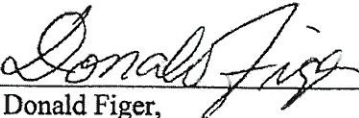**Kimberly Kolb**

**Rochester Institute of Technology**

**3 March 2014**
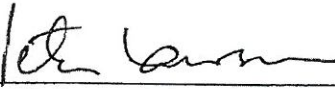
# Approvals

**Released by**

_____       6/4/14
Dr. Donald Figer,
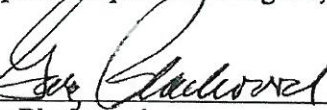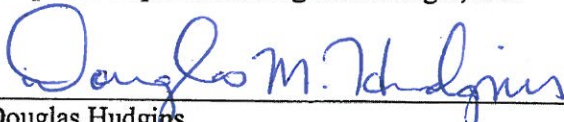Principal Investigator

**Approved by**

_____       6/23/14
Peter R. Lawson,
Exoplanet Exploration Program, Chief Technologist, JPL

_____       6/29/14
Gary Blackwood
Exoplanet Exploration Program Manager, JPL

_____       6/25/14
Douglas Hudgins
Exoplanet Exploration Program Scientist, NASA HQ

_____       6/25/14
John Gagosian
Exoplanet Exploration Program Executive, NASA HQ

# Table of Contents

# TDEM Milestone Report:
# A Photon-Counting Detector for Exoplanet Missions

## 1. Objective

In support of NASA's Exoplanet Exploration Program and the ROSES Technology Development for Exoplanet Missions (TDEM), this report describes the accomplishment of the TDEM Milestone for *A Photon-Counting Detector for Exoplanet Missions*, specifies the methodology for computing the milestone metric, establishes the success criteria against which the milestone will be evaluated, and reports on the experimental demonstrations.

## 2. Introduction

This Technology Milestone serves to gauge the developmental progress of technology for a space-based coronagraph mission that would detect and characterize exoplanets, and the mission's readiness to proceed from pre-Phase A to Phase A. This milestone addresses measurement of the characteristics of a new photon counting array detector. The detector is a 256×256 Geiger-Mode Avalanche Photodiode (GM-APD) focal plane array that provides zero read noise, ultra-high dynamic range, and highly linear response over the relevant flux range of interest. It will deliver significant enhanced performance over existing technologies for a planet finding spectrograph, as a wavefront sensor, and for an imager.

JPL document D-66493, "A Photon Counting Detector for Exoplanet Missions," is the Technology Milestone White Paper for this project. It includes an overview of the device design and fabrication, as well as the radiation testing program. The White Paper presents a detailed description of the milestone procedure for testing the devices, as well as specific success criteria for the project. The approach for accomplishing the milestone has been to fabricate, irradiate, and test photon-counting detectors in performance metrics relevant to *NASA* exoplanet missions. The low-fill-factor version of these devices were partially advanced from TRL3 toward TRL4 with respect to some aspects of environmental exposure characterization, The testing followed the criteria established in NASA NPR-7120.8 App. J, though since the start of this project NASA has updated its procedures to NPR-7123.1B.[1] In particular, it demonstrates the performance of GM-APDs in the presence of a radiation environment that is representative of a typical exoplanet mission.[2] The TPF-C Flight Baseline Mission Design[3] defines exoplanet mission system characteristics for the purposes of this effort. The requirement for this milestone reads as follows:

---

[1] http://nodis3.gsfc.nasa.gov/displayDir.cfm?Internal_ID=N_PR_7120_0008_&page_name=AppendixJ

[2] We regard radiation effects as the most critical area of concern for this technology for advancement to TRL 5, although the technology must ultimately also pass testing in the presence of other environmental conditions, e.g. heat and vibration.

[3] http://planetquest.jpl.nasa.gov/TPF-C/TPFC-MissionAstro2010RFI-Final-2009-04-01.pdf

Milestone: Measure Performance of a Photon-Counting 256×256 Focal Plane Array after Radiation Exposure

*Measure the following characteristics of a single-photon counting 256×256 focal plane array detector: dark current, intra-pixel sensitivity, total quantum efficiency, afterpulsing, persistent charge, and crosstalk. The measurements will be made before and after 50 krad (Si) ~60 MeV proton irradiation. Important performance parameters include read noise, dark counts, and total quantum efficiency.*

The detector design uses an in-pixel charge amplifying circuit that converts each absorbed photon into a relatively large voltage signal that can easily be detected by a CMOS readout circuit. The amplification is provided by a GM-APD that accelerates photo-generated charge in a region of high electric field. Each photodiode is individually bump-bonded to a silicon readout circuit. The circuitry in each pixel registers the arrival of a photon and resets the photodiode so that it is ready to absorb another photon in ~100 ns. [4] A counter in each pixel accumulates photon absorption events. The readout circuit multiplexes the digital output of the counters for each pixel through serial output registers and digital buffers.

## 2.1 Photon-Counting Detector Design

An overview of the detector design and operation is provided in the White Paper for this project. For reference, a brief summary of the internal architecture of the GM-APD pixels is reproduced here.

Figure 1 shows a cross-section of two versions, one using a low-fill-factor (LFF) design and the other using a high-fill-factor (HFF) design. Both designs are intended to be used in a backside-illuminated configuration. On the right of the figure, the shallow portion of the stepped p+ implant separates the absorber and multiplier portions of each detector. The step lowers the electric field at the edges of the diode, preventing edge breakdown and forming a guard ring to collect surface-generated dark current without multiplying it. The deep portion of the implant, which is partially undepleted, prevents the guard ring from collecting photoelectrons generated in the absorber; as indicated in the figure, these photoelectrons reach a nearby multiplier region by a combination of diffusion and drift.

---

[4] This is a relatively long time when considering the very low flux levels expected for an exoplanet mission. For instance, in spectroscopic mode, the flux is ~0.2 photons/s.
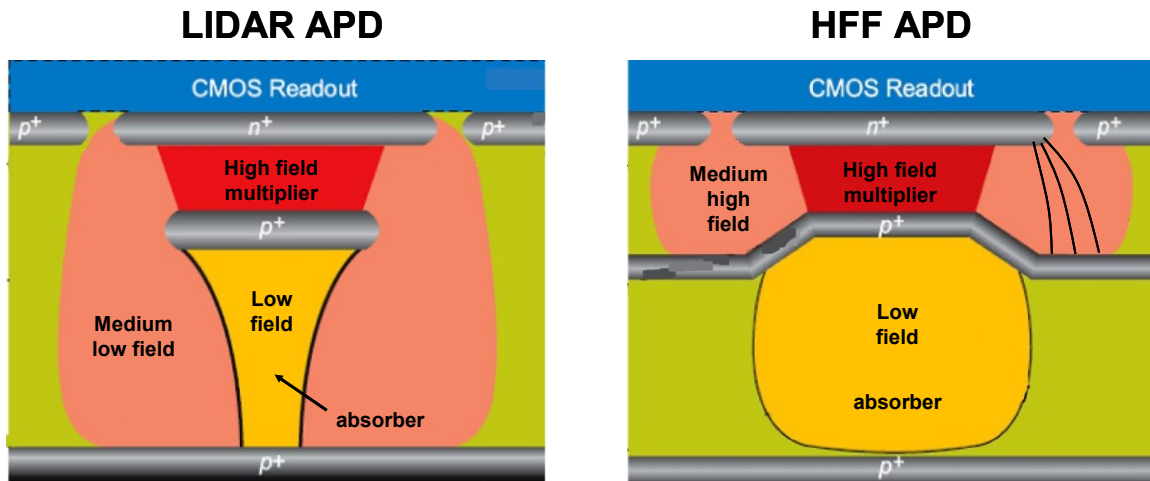
**LIDAR APD**

**HFF APD**

*Figure 1. Cross-sections of two APD designs, one using a low-fill-factor (LIDAR) design suitable for LIDAR (left) and the other using a high-fill-factor (HFF) design suitable for imaging applications (right). Photons are absorbed in the "absorber" regions. Charge is multiplied in the "multiplier" regions.*

## 2.2 Radiation

Justification for radiation testing, as well as the radiation testing plan, is presented in the White Paper.

The radiation testing program for this project assumes a five year mission lifetime and a spacecraft location at L2, given that the majority of proposed exoplanet missions would be located there.[5] At a location of L2, we expect the cumulative dose to be ~5 krad (Si) for a five year mission lifetime and average solar activity.

# 3. Milestone Procedure

The milestone procedure is described in the White Paper. It describes the original testing plan and procedures for characterizing the GM-APD array devices. The original testing plan includes validation of zero read noise and measurement of dark count rate, intra-pixel sensitivity, quantum (or photon detection) efficiency, afterpulsing, persistent charge, and crosstalk. It also gives an overview of the conversion of count rate to quantum units and dead time correction. These concepts are explained in more detail in section 5.

# 4. Success Criteria

The following are the required elements of the milestone demonstration, per the White Paper.

**4.1.**     One or more Geiger-Mode Avalanche Photodiode arrays will be fabricated with a high fill-factor, as described in Section 2.3, with a 256×256 format and a pixel size of 25 microns.

Rationale: *The high-fill factor and 256×256 array demonstrates the intended format of the GM-APD typical of use for exoplanet missions.*

---

[5] Taken from the "Exoplanet Forum 2008" (http://exep.jpl.nasa.gov/exep_exfPresentations.cfm)

**4.2.** One GM-APD array described in 4.1 will be tested following the procedure described in in the White Paper to demonstrate a baseline photon detection sensitivity of 35% at 350 nm, 50% at 650 nm, and 15% at 1000 nm.

Rationale: *This provides evidence that the device is functioning nominally at a baseline performance level. Stringent requirements are not placed on the photon detection efficiency, because the goal of this milestone is specifically to demonstrate operation with zero read noise.*

**4.3.** Elements 4.1 and 4.2 must be satisfied for one or more GM-APDs that demonstrate zero read noise, as per the procedure detailed in 3.2.1.

Rationale: *A demonstration of zero read noise is the primary goal of this milestone.*

**4.4.** One GM-APD, having previously complied with Elements 4.1–4.3, will be exposed to high energy radiation and tested. The radiation will be in the form of a proton beam, having ~63 MeV particles (+/-10%), with spatial uniformity of +/-10% across the detector, absolute calibrated flux levels of +/-10%, delivered in dose increments no greater than 1 krad (Si), and total doses up to 50 krad (Si).

Rationale: *Radiation testing of the arrays is a crucial step in preparing the devices for flight readiness. Although the results of the tests will be provided, it is the completion of the tests themselves, not a specific performance threshold that marks the completion of this milestone effort. An improved design based on these tests will be the subject of a continuing future effort.*

**4.5.** The pre-radiation tests described in 4.2 and the post-radiation tests described in 4.4 shall be repeated three times without warming up the detector.

Rationale: *The repeated measurements will demonstrate the stability of the performance of the device.*

# 5. Results

Pre- and post-radiation testing was designed based on the goals outlined in this paper. Testing includes characterization of dark count rate (DCR), afterpulsing probability, photon detection efficiency (PDE), persistent charge, intra-pixel sensitivity (IPS), and crosstalk. Read noise is noise in the estimated signal added by the readout electronics. The White Paper described an experiment to measure the read noise. A more robust experiment is to count the number of false positives and negatives produced by the readout circuit in the absence of any other effects. This experiment was part of early device validation, and it gave zero false events out of 65536x5000 trials.

Minor modifications were made to other experiments as detailed in the White Paper, and each results section outlines the experiment setup and procedure actually used for each test. Each experiment was repeated three times. Post-radiation PDE and persistent charge were not measured due to a lack of time.

Of the five success criteria listed in section 4, three were met. The first criterion, the fabrication of a HFF device, was met, but testing on the device could not be completed due to extraordinary crosstalk (see section 5.1.6). Design improvements for reducing crosstalk have been implemented in devices that are currently being fabricated.. Therefore, the results from LFF devices (S45, S47, and S51) are presented. The second criterion, to demonstrate baseline photon detection efficiency (PDE), was not met. The third criterion was met, as the detectors demonstrated zero read noise. The fourth criterion was not met, as testing was done with LFF

instead of HFF devices and two of the tests (post-radiation PDE and persistent charge) were not completed. LFF detectors have much lower PDE than HFF detectors due to their decreased active area (see section 5.1.5). Despite their low PDE, however, the LFF detectors are deemed useful for the investigation of radiation effects, since we expect the most significant changes in detector performance to be increases in dark count rate (DCR) and afterpulsing probability. The last criterion, to repeat experiments three times without warming the detector, was met.

For these detectors, the exposure time is the total gate time, which is accumulated incrementally over a series of detection periods. Each detection period contains a user-defined gate time and hold-off time. The gate time is the period during which a pixel can avalanche. In the following sections, the gate time is referred to as $t_{gate}$, the hold-off time is referred to as $t_{hold-off}$, and the exposure time is $t_{gate}$ multiplied by the number of gates. At the beginning of a gate, a short (~0.1 μs) arm pulse is asserted to increase the bias above the breakdown voltage. During the beginning of the arm pulse, the pixel cannot register an avalanche, but this is considered to be a negligible contributor to dead time. If an avalanche occurs during a gate, the bias is decreased below breakdown to quench the avalanche. Only one avalanche can be recorded per gate because the pixel cannot avalanche after the voltage is decreased. At the end of the gate, the state of the pixel is recorded (a 1 or a 0, where a 1 means that an avalanche was registered during the gate), and then a short (~0.1 μs) disarm pulse is asserted to decrease the bias below the breakdown voltage for all pixels that did not avalanche during the gate. This ensures that no avalanches occur during the hold-off time, which immediately follows the previous gate and lasts until the beginning of the next gate. The output from the detectors is the total number of ones for each pixel.

Results are presented as a function of applied overbias, rather than external applied bias. Overbias is the excess bias applied above the breakdown voltage for a specific device, and is controlled by the user. Comparisons between detectors are only valid if they are tested using the same overbias.

## 5.1 Pre-Radiation Characterization

Pre-radiation testing was completed in September, 2013. DCR, afterpulsing probability, PDE, intra-pixel sensitivity (IPS), and crosstalk were measured. The results for each experiment are presented below.

### 5.1.1 Dark Count Rate (DCR)

DCR is the rate of counts generated in the absence of light. In this paper, DCR is corrected for dead time and the experiments to measure it are designed to minimize counts from afterpulsing. The intention is that the results reflect what is commonly referred to as dark current. As such, the units of DCR are expressed as electrons/s/pixel (Hz). The original testing plan includes DCR measurements with a total exposure time of one hour at each temperature. In order to minimize afterpulsing, the hold-off time was kept long (~5 ms), which kept the duty cycle low. Given the low duty cycle, an hour was a prohibitively long exposure time. With 10 μs gate times and 5 ms hold-off times, a cumulative gate time of 1 hour would take 20.9 days. Instead, the necessary exposure time was set by calculating the number of gates required for the desired SNR. The SNR of a measurement is proportional to the square root of the total number of gates. With this in mind, the number of gates was changed to 1 million, equivalent to an on-source exposure time of 10 s. The minimum SNR for the entire DCR experiment was 14 using these settings.

The probability of an avalanche in a single gate (P) is the number of ones divided by the number of gates. Since the rate at which electrons enter the multiplication region is Poissonian, the Poisson probability model can be used to solve for the mean electron flux, given P and the $t_{gate}$. Equation 1 shows the relationship between P, $t_{gate}$, and the DCR ($\lambda_e$). Note that Equation 1 cannot be used if the afterpulsing probability is not zero. Afterpulse counts are not Poissonian, and so they cannot be included in $\lambda_e$.

$$P = 1 - e^{-\lambda_e t_{gate}}$$

$$\lambda_e = \frac{-\ln(1 - P)}{t_{gate}}$$

*Equation 1*

The figures below show the results from the DCR experiment for each LFF device (S47, S51, and S45). The error bars on the plots in this report show the standard deviation of the measured results. The expected trend for a silicon substrate is the doubling of dark current (which is proportional to DCR) roughly every 8 K, but these devices show doubling roughly every 17 K. This shallow slope may be caused by biasing effects. Although the bias is adjusted with temperature to account for the change in breakdown voltage, there is no way to know if the adjustment compensates for the change. Additionally, the breakdown voltage for each pixel in a detector array is not uniform. This is likely due to processing non-uniformity across the production wafer, specifically implant depths and doses, as well as local defects in the substrate. This non-uniformity in breakdown voltage, combined with changes in the shape of the multiplication region due to biasing, leads to uncertainty in the overbias.
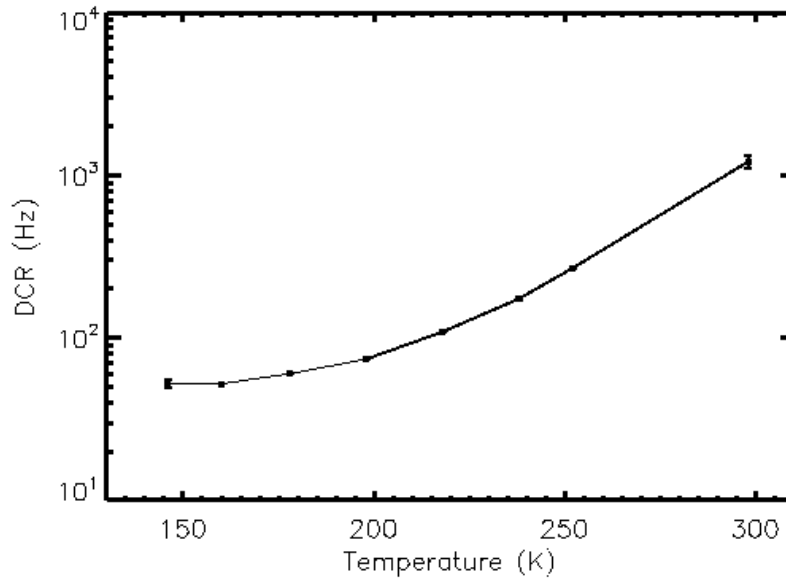


Figure 2. This plot shows median DCR vs. temperature for S47. Longer arm periods were used to ensure that afterpulsing was insignificant at lower temperatures.

*Figure 3. This plot shows median DCR vs. temperature for S51. Longer arm periods were used to ensure that afterpulsing was insignificant at lower temperatures.*



*Figure 4. This plot shows median DCR vs. temperature for S45. Longer arm periods were used to ensure that afterpulsing was insignificant at lower temperatures.*
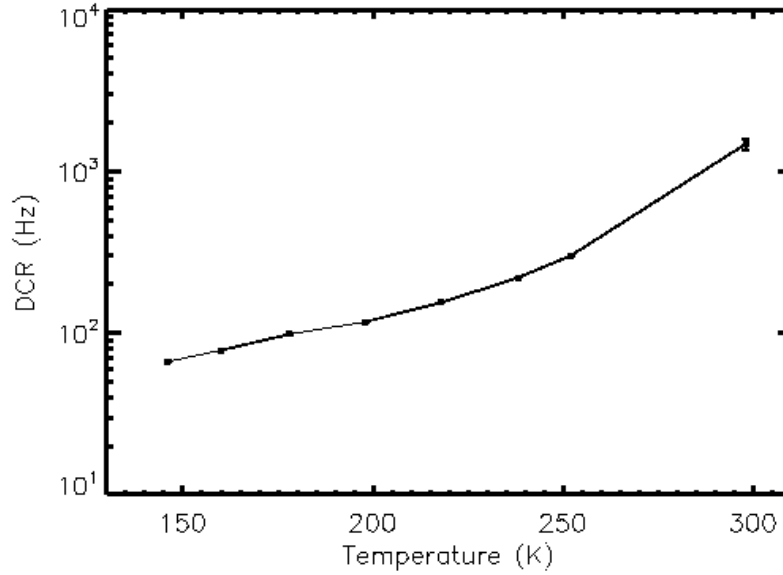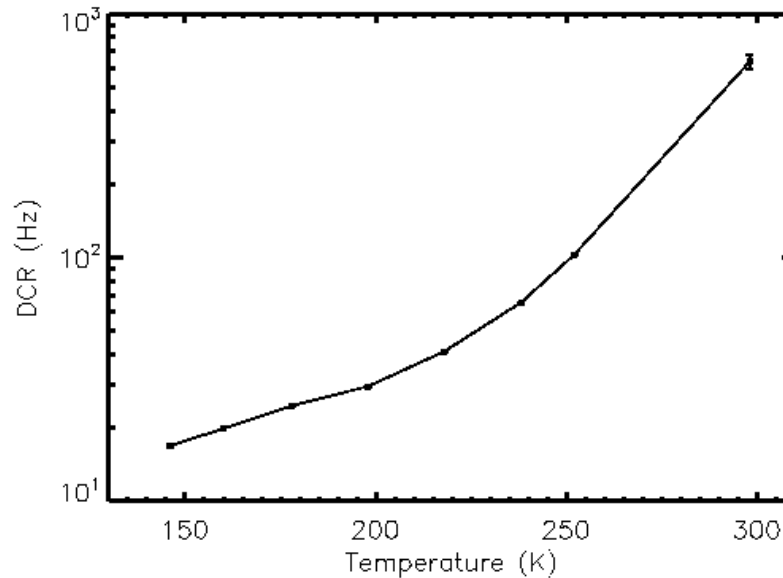
MIT Lincoln Laboratory characterized the dark count rate of high-fill-factor arrays. As suggested by single-device test data, dark counts can arise from mechanisms other than thermally-generated dark current. At sufficiently high overbiases, one can observe many crosstalk-induced events, which elevates the apparent dark count rate. This effect is particularly severe for high-fill-factor devices and the analysis of dark count data on such devices will be discussed below in the section on crosstalk.

### 5.1.2 Afterpulsing Probability

Afterpulsing is an increase in count rate following an avalanche in the same pixel. Afterpulsing is often caused by traps, which are energy states that exist only around material

defects in the detector substrate. Instead of being collected, charge can become "trapped" in these energy states and released a random amount of time later, depending on the specific trap lifetime of the trap. The time at which charge leaves the trap is random and exponentially distributed. The trap lifetime is the average amount of time charge takes to leave the trap state. The original testing plan required biasing a single pixel in the array, and firing a short (10 ns) laser pulse at the pixel. Afterpulsing probability could be calculated using the auto-correlation function of the gates following the pulse.

However, a single pixel cannot be armed due to constraints in the ROIC. We updated the experiment method to accomplish the same objective. The updated method requires measuring the avalanche probability at various hold-off time settings. At hold-off times that are much longer than the trap lifetime of traps in the detector, afterpulsing probability is near zero. By taking data at a very long hold-off time, we estimate that measured DCR ($\lambda_e$) at that hold-off time is not affected by afterpulsing. The afterpulsing probability at shorter hold-off time settings were determined using a theoretical model for avalanche probability and the zero afterpulsing DCR ($\lambda_e$). In this case, afterpulsing probability ($p_{aft}$) is the probability of an afterpulse carrier initiating an avalanche during a gate, given an avalanche in the previous gate. This model assumes that the state of a gate is only dependent on the state of the gate immediately before it. This assumption allows for the representation of avalanche probability (P) for each gate in an infinite series (n=0,1,2,…). With the use of the Maclaurin series identity, that infinite series simplifies to the closed-form solution in Equation 2. It is important to note that Equation 2 assumes that there are no incident photons, though it would be possible to calculate $p_{aft}$ if the photon signal were constant by substituting (PDE·$\lambda_p$+ $\lambda_e$) for $\lambda_e$.

$$P = \frac{1 - e^{-\lambda_e t_{gate}}}{1 - p_{aft}e^{-\lambda_e t_{gate}}}$$

$$p_{aft} = \frac{1 - e^{\lambda_e t_{gate}}(1 - P)}{P}$$

*Equation 2*

Figure 5 shows avalanche probability (P) vs. gate fluence for various values of $p_{aft}$. Gate fluence is the number of electrons per pixel per gate that are capable of initiating an avalanche. The avalanche probability values are calculated using Equation 2. Note that the avalanche probability converges at small and large gate fluence values. When gate fluence is low, any additional avalanches from afterpulsing are unlikely because the avalanche probability is very low to begin with. At high gate fluence, afterpulse events are often coincident with avalanches that would have occurred because of the gate flux. Figure 5 also shows that the change in avalanche probability is not linearly proportional to afterpulsing probability.
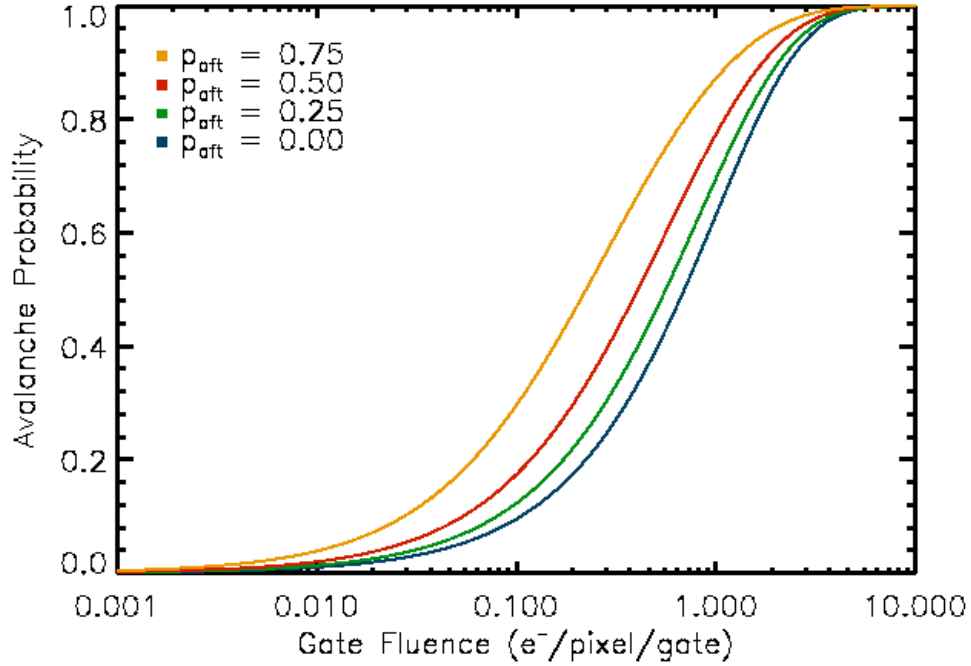
*Figure 5. This plot shows avalanche probability vs. gate fluence (the number of electrons entering the multiplication during a gate that would initiate an avalanche) for various afterpulse probabilities ($p_{aft}$).*

Figure 6 - Figure 8 show afterpulsing probability ($p_{aft}$) vs. hold-off time S47, S51, and S45. Trap lifetimes were calculated by fitting an exponential decay function to the $p_{aft}$ values at each temperature. They range from 3 μs – 10 μs at temperatures below 160 K and are generally less than 1 μs at warmer temperatures. For all detectors, a hold-off time of at least 1 ms will ensure that $p_{aft}$ is less than 0.01% at the temperatures below 160 K, while a hold-off time of 10 μs is sufficient at warmer temperatures. Afterpulsing probability increases as the trap lifetime lengthens at colder temperatures. To achieve a duty cycle of 90% with an afterpulsing probability of < 0.01%, a gate width of 90 μs would be necessary at temperatures above 160 K. At temperatures below 160 K, a gate width of 9 ms would be necessary.
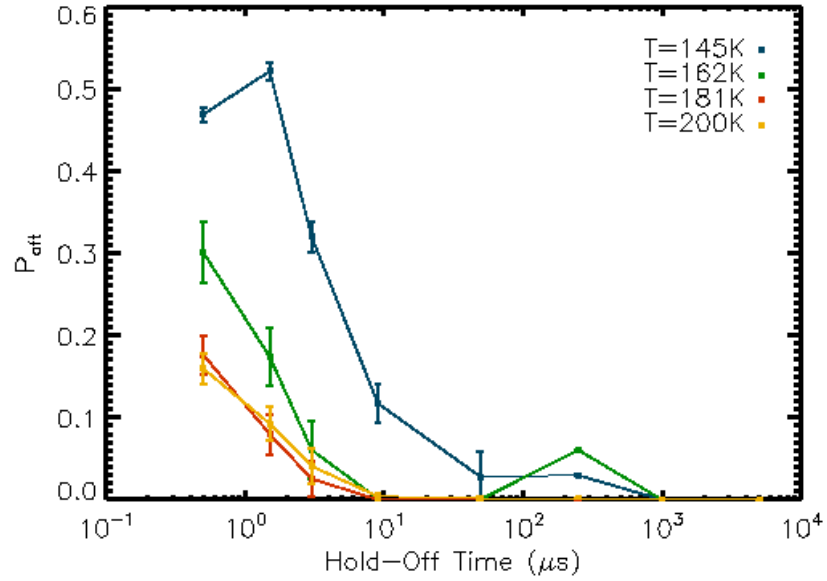
Figure 6. Median afterpulsing probability vs. hold-off time at multiple temperatures is shown for S47. The gate time for this experiment is 1 μs.



Figure 7. Median afterpulsing probability vs. hold-off time at multiple temperatures is shown for S51. The gate time for this experiment is 1 μs.

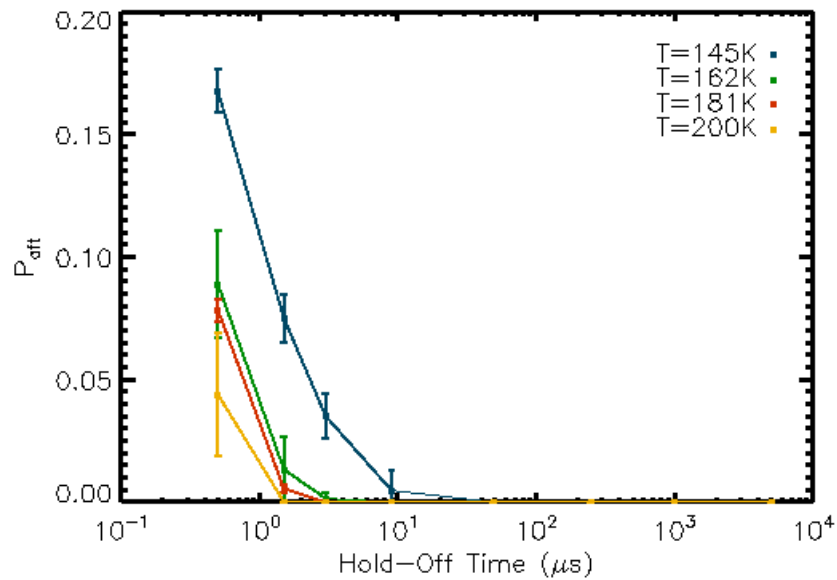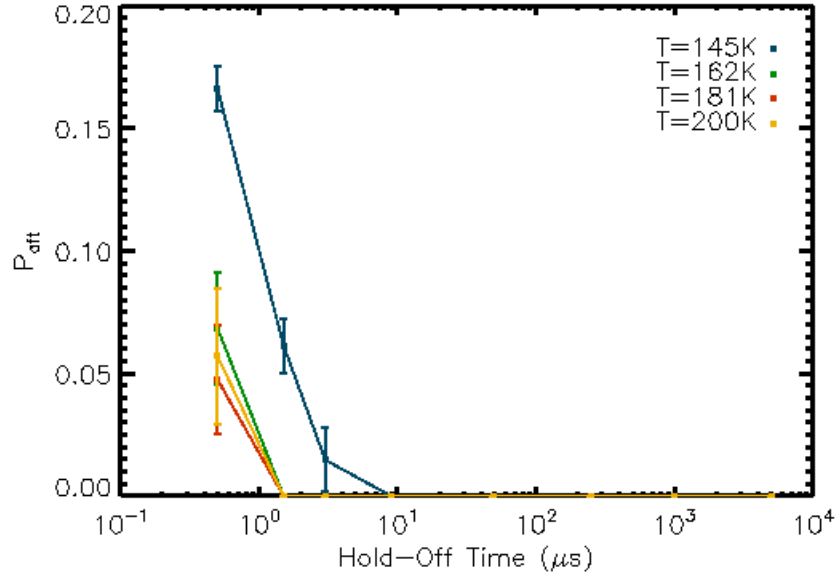*Figure 8. Median afterpulsing probability vs. hold-off time at multiple temperatures is shown for S45. The gate time for this experiment is 1 μs.*

### 5.1.3  Photon Detection Efficiency (PDE)

PDE is the inferred photo-generation rate divided by the incident photon rate. PDE is equivalent to quantum efficiency (QE) multiplied by the avalanche initiation probability. The testing outline requires measuring PDE from 300 nm to 1100 nm.

The PDE of a device is very dependent on overbias because overbias increases the avalanche initiation probability. Figure 9 shows PDE at 520 nm as a function of overbias.
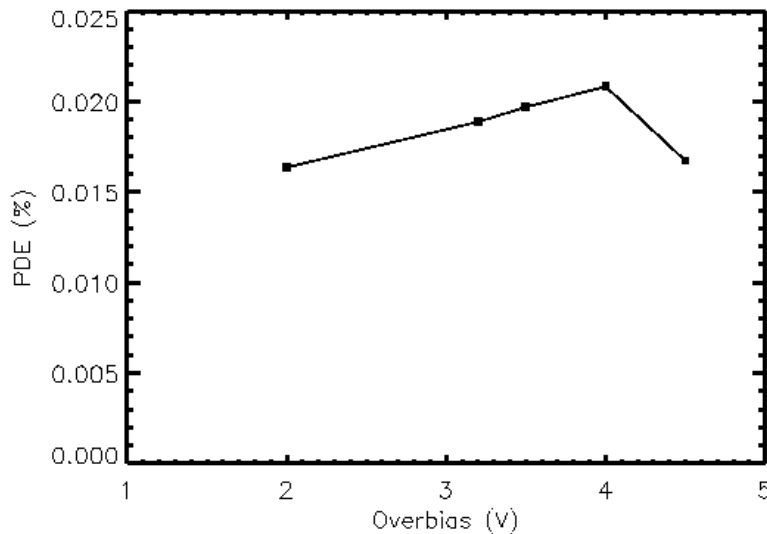


*Figure 9. PDE (%) vs. overbias for a single pixel on S45. The wavelength setting was 520 nm. PDE increases with overbias until a certain point at which the multiplication region begins to be pinched off by the high electric field in the absorber region.*

DCR increases with overbias due to increased avalanche initiation probability as well. In order to avoid high DCR, PDE was measured with a moderate overbias of 2 V. It is interesting to note that HFF devices from the same production wafer, at similar overbiases, have peak PDEs in

11

the 15% range, while PDE for the LFF devices peaks below 1%. This is due to the volume of the active area per pixel, which is much greater in the HFF devices.

Equation 3 shows the expression for the number of photo-generated electrons entering the multiplication region during a gate that can initiate an avalanche. The expression is a function of avalanche probability, DCR, and $t_{gate}$. The derivation assumes that afterpulsing probability is negligible.

$$P = 1 - e^{-t_{gate}(\lambda_p + \lambda_e)}$$
$$\lambda_p = \frac{-\ln(1 - P)}{t_{gate}} - \lambda_e$$

*Equation 3*

A calibrated photodiode (UV-enhanced Si) was used to determine the number of photons incident on the detectors. This was done by measuring the flux inside of an integrating sphere illuminated by a monochromator. In order to account for changes in flux at the detectors vs. the calibrated photodiode, an experiment was run with two diodes simultaneously: one in the integrating sphere position and one inside the dewar at the same position as the detectors. We then calculated the ratio of photon flux between the two photodiodes and used that ratio to calculate the flux on the detectors based on the diode readings inside the integrating sphere. Equation 4 shows the expression for PDE in terms of $\lambda_p$ (electrons/gate/pixel), $S_D$ (diode signal in photons/s/mm$^2$), K (the ratio of photons incident on the detectors to photons incident on the calibrated diode in the integrating sphere), $A_{pix}$ (the area of a pixel in mm$^2$), and $t_{gate}$.

$$PDE = \frac{\dfrac{\lambda_p}{t_{gate} \cdot A_{pix}}}{S_D \cdot K}$$

*Equation 4*

For each new wavelength setting, the mechanical parts of the monochromator move, which causes the background light level to change at each wavelength. Therefore, dark exposures were taken at each wavelength setting to account for the changes in background light level. $\lambda_e$ was calculated from each dark exposure and subtracted from the total number of electrons detected to calculate $\lambda_p$ as in Equation 3. Equation 4 was then used to calculate the PDE for each pixel.

The maximum SNR occurs at P=0.797, which can be arranged by setting the gate time, assuming that the photon flux is constant for all gates. In order to ensure statistically relevant results, the gate time was optimized for four separate wavelength intervals based on the signal level expected at the detectors. Choosing a minimum SNR of 3, minimum and maximum gate times were calculated using extrapolated values for photon flux, PDE, and DCR from a preliminary experiment. Figure 10 shows the ideal gate time vs. wavelength for the PDE experiment, while the minimum and maximum gate times at each wavelength are the error bar bounds. The green line shows the gate times that were chosen for the experiment.
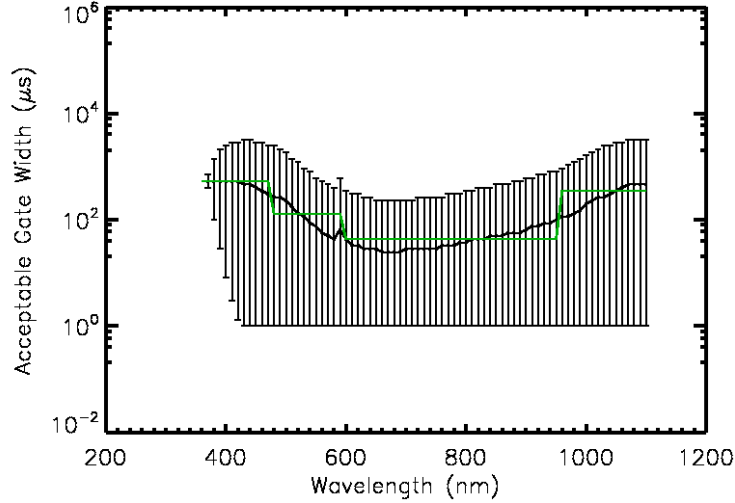
*Figure 10. This plot shows the ideal gate time (solid black line) vs. wavelength for the PDE experiment. The ideal gate time gives an avalanche probability of 0.797 per gate. The minimum and maximum gate times (error bars) are calculated by assuming a minimum SNR of 3, with a minimum allowable gate time of 1 μs. The green line shows the chosen gate times at each wavelength for the experiment.*

Figure 11 shows the expected SNR vs. wavelength for the PDE experiment. The expected SNR is calculated using the chosen gate time values from Figure 10 and extrapolated values for photon flux, PDE, and DCR from a preliminary experiment. Some data points for S47 fall below an expected SNR of 3 at wavelengths less than 400 nm because S47 has higher DCR than the other two detectors. The same gate time setting is applied to all three detectors, even though they each have different DCR levels, and the gate times chosen yield greater than an SNR of 3 on average.
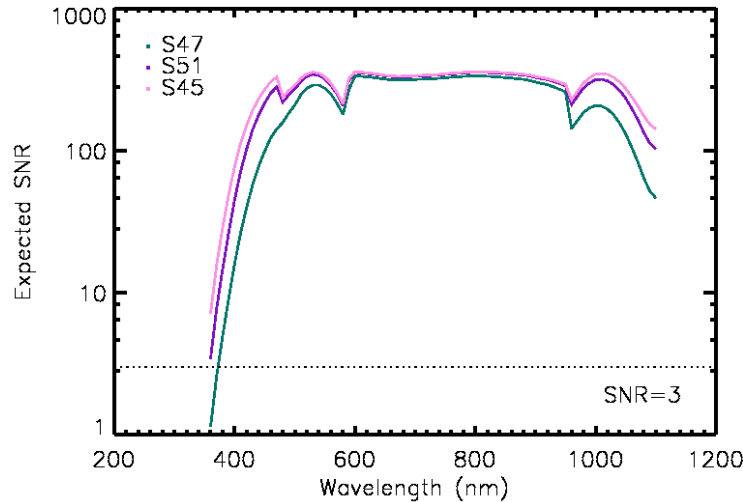


*Figure 11. This plot shows the expected SNR vs. wavelength for each detector. Expected SNR is calculated based on chosen gate times and extrapolated values for photon flux, PDE, and DCR from a preliminary experiment.*

The results presented in Figure 12 were taken at a temperature of 130 K. For all three detectors, the short-wavelength cut-off was ~480 nm and the long-wavelength cut-off was ~1.06 μm. The PDE results of the detectors are in good agreement across wavelength range of

the experiment, with roughly 9% standard deviation between them at peak PDE. The distribution of PDE values for individual pixels is similar. For S47, 46% of pixels are within 10% of the median, 26% are within 5% of the median, and 7% are dead or hot pixels. For S51, 34% of pixels are within 10% of the median, 19% are within 5% of the median and 16% are dead or hot pixels. For S45, 28% of pixels are within 10% of the median, 12% are within 5% of the median, and 20% are dead or hot pixels.
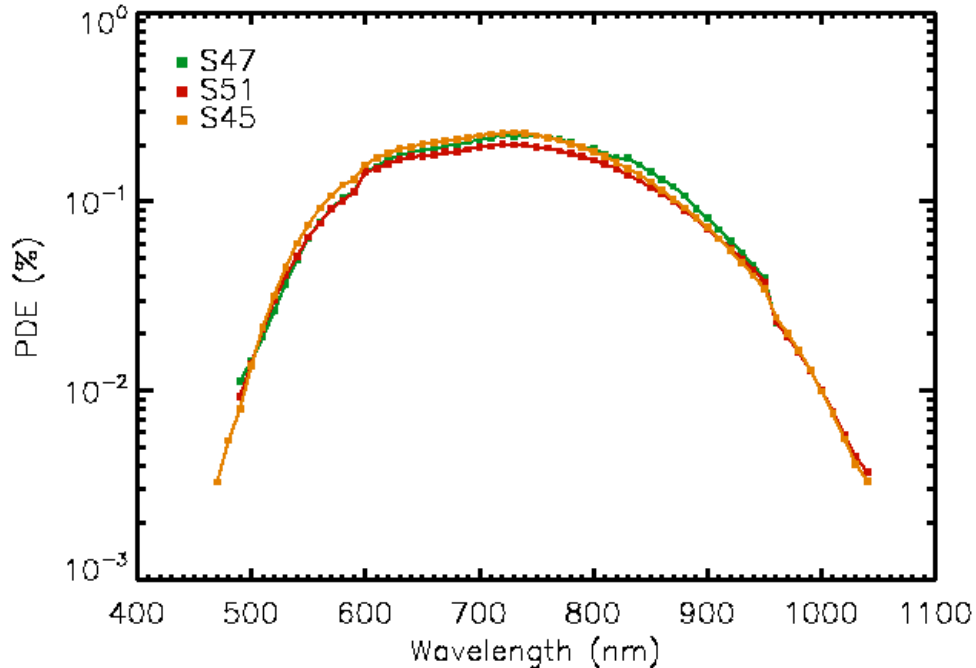


*Figure 12. This figure shows median PDE (%) vs. wavelength for each detector.*

Figure 12 shows the median PDE for each detector without correcting for fill factor. This PDE is equivalent to the mean of the IPS function (see section 5.1.5) for the pixel. For these detectors, the IPS function can be fit very well with a Gaussian curve that peaks in the center of the pixel. Thus, the measured PDE would be much higher if the signal were concentrated in the center of the pixel. The IPS function and the measured PDE over the whole pixel can be used to calculate the peak sensitivity at the center of the pixel. Since the IPS function is normalized, the mean amplitude of the Gaussian curve is a scaled version of the measured PDE. The defining characteristic of a normalized Gaussian curve is the full width at half maximum (FWHM), the width of the curve when the amplitude is 50%. The ratio of the mean amplitude to the measured PDE is the peak sensitivity. This peak sensitivity is 4.75% at 720 nm, using the FWHM values calculated in section 5.1.5.

### 5.1.4 Persistent Charge

Persistent charge is charge that becomes trapped in a pixel during an illuminated gate and later becomes liberated and counted in subsequent gates. The original testing plan requires illuminating the devices at three different flux settings and then measuring the signal from each detector after the light source is turned off. The original requirement was 2000 s of exposure time under the illuminated conditions, but this CCD-based metric is not necessarily relevant for these devices. Since intensity is measured as a function of avalanche probability by these detectors, they do not saturate in the way that an analog device does. Instead of reaching a full

well, the avalanche probability approaches (but never reaches) 1. When the number of gates is less than $\frac{1}{P}$, the measured probability can be 1, which means that an avalanche occurred in every gate. This is considered saturation for GM-APDs in photon-counting mode. The plan was changed to take 2000 gates of dark data, take 50,000 gates under saturated conditions, and then take dark data until the measured signal returns to the pre-illuminated level. To increase the temporal resolution, data was taken in sets of 100 gate exposures. $t_{gate}$ was 450 μs and $t_{hold-off}$ was 1000 μs; the duty cycle was 31%. The per-gate fluence was 3375 photons/gate. Because no persistence was measured at an avalanche probability of 1, no data was taken at lower probabilities.

Persistent charge results for S47 presented in Figure 13. Data for S51 and S45 were taken, but show the same results and would be redundant. No increased signal level was measurable after saturation on this time scale. This was expected because of the unique detection cycle of the devices. During the $t_{hold-off}$, the bias across the pixel is decreased below the breakdown voltage, but is still significant. The remaining bias evacuates carriers in the absorption and multiplication regions, which prevents their detection even if the carrier lifetime is long.
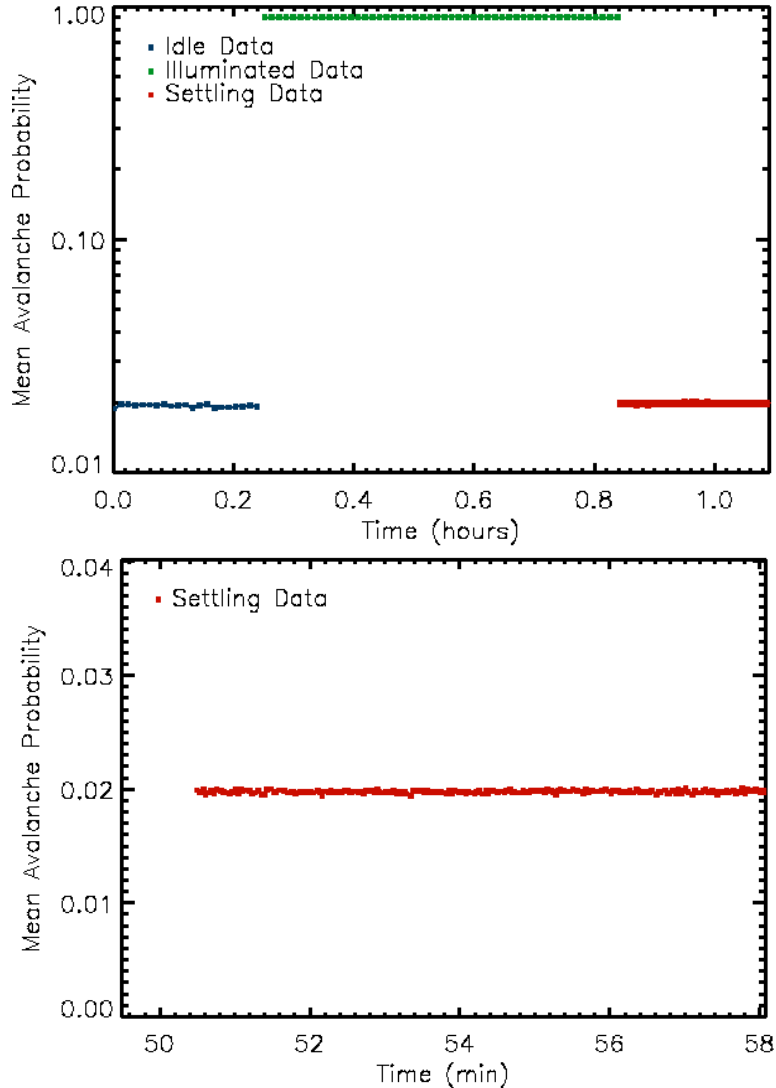
*Figure 13. This figure shows mean avalanche probability vs. time. The top plot shows results from the full experiment, complete with idle, illuminated, and settling measurements. The bottom plot shows just the settling data on a finer scale to emphasize the lack of increased signal level after saturation.*

### 5.1.5 Intra-Pixel Sensitivity (IPS)

IPS is the photon detection efficiency as a function of location inside a pixel. Ideally, the IPS function would be constant across the entire pixel, but for these LFF GM-APDs, the active area is concentrated at the center of each pixel and can be modeled as a 2D Gaussian function. The original testing plan requires measuring IPS at multiple pixels by projecting a small pinhole image onto the detectors with a FWHM of 2 μm. The spot was moved through a 2x2 pixel grid with 1/10th pixel spacing (2.5 μm), with exposures at each grid location. Contour plots of the relative signal level as a function of spot location are reported as the IPS of the pixels measured.

Reported values for FWHM are corrected for the expected size of the laser spot scanned across the pixels. Generally, the FWHMs of the sensitivity curves for each detector are consistent between pixels in the detector, but vary between detectors. Values range from 5 μm to 15 μm, or 3.4%-29.0% of the total pixel area. Since the measured overall PDE values for each detector are

very similar, the IPS functions should also be similar. The size of the laser spot is highly dependent on the focus, so we hypothesize that the variance in FWHM between detectors is a function of the variance of the spot size when moving the spot projector and re-focusing. The smallest spot size we attained was ~4 μm.

Fill factor is calculated from the IPS function by integrating over the normalized IPS function (corrected for the laser spot size) and dividing the result by the volume of a 3D rectangle with height equal to 1 and length and width equal to the pixel dimensions. The fill factors for S47, S51, and S45 are 18.4%, 37.0%, and 4.8%, respectively.

Figure 14-Figure 16 show the measured IPS of two pixels on one detector as a function of location within the pixels. Note that the scan area is 2x2 pixels, but each plot only shows the signal from one pixel during the scan.

Figure 14. IPS results from S47 from two separate pixels are shown. The centers of the pixels are in the central ring on each plot. In both cases, the FWHM is 10.2 μm, containing 13.1% of the total pixel area. The fill factor of these pixels is 18.4%.

*Figure 15. IPS results from S51 from two separate pixels are shown. The centers of the pixels are in the central ring on each plot. In both cases, the FWHM is 15.2 μm, containing 29.0% of the total pixel area. The fill factor of these pixels is 37.0%.*
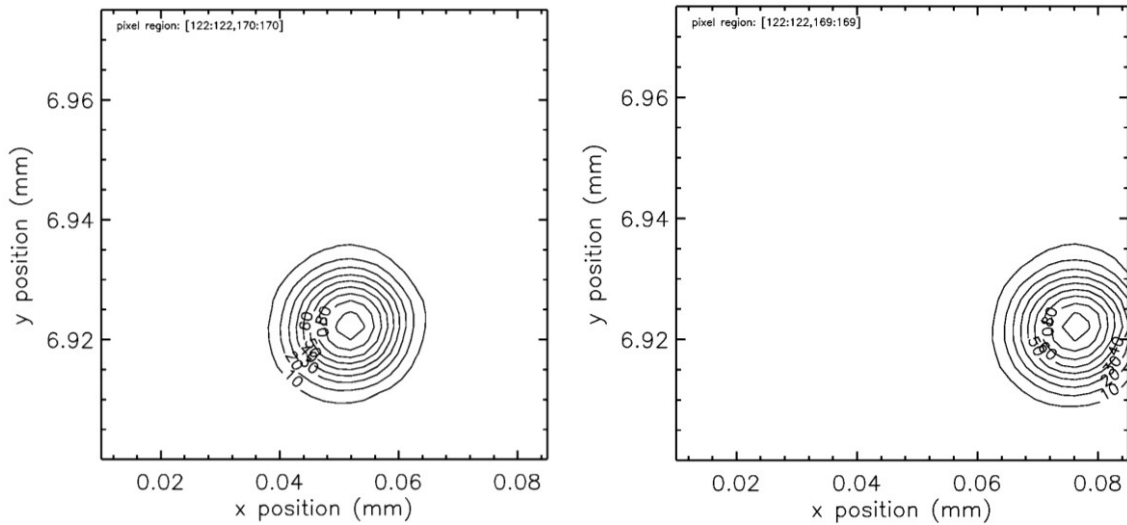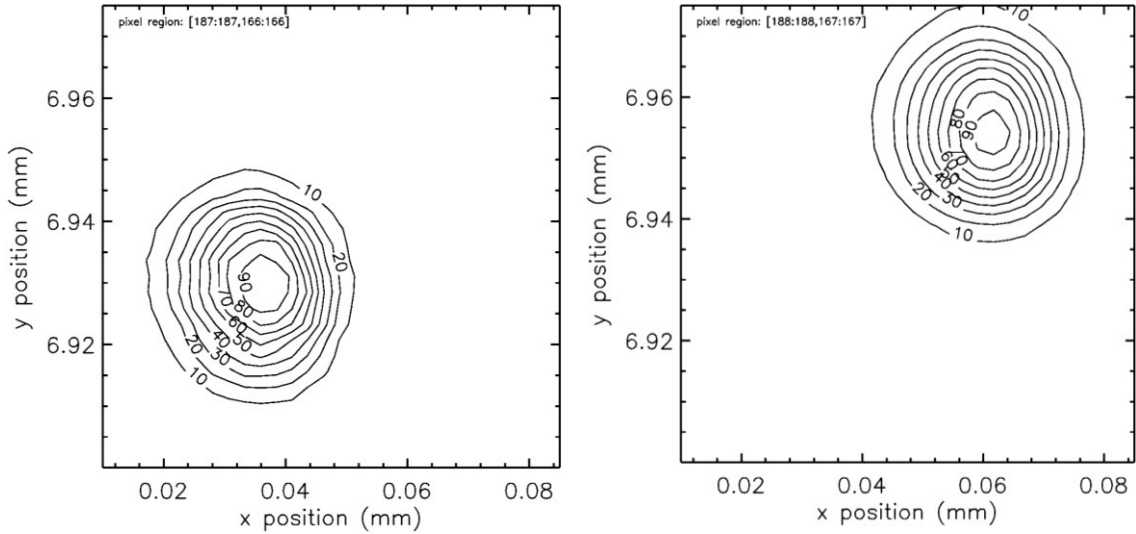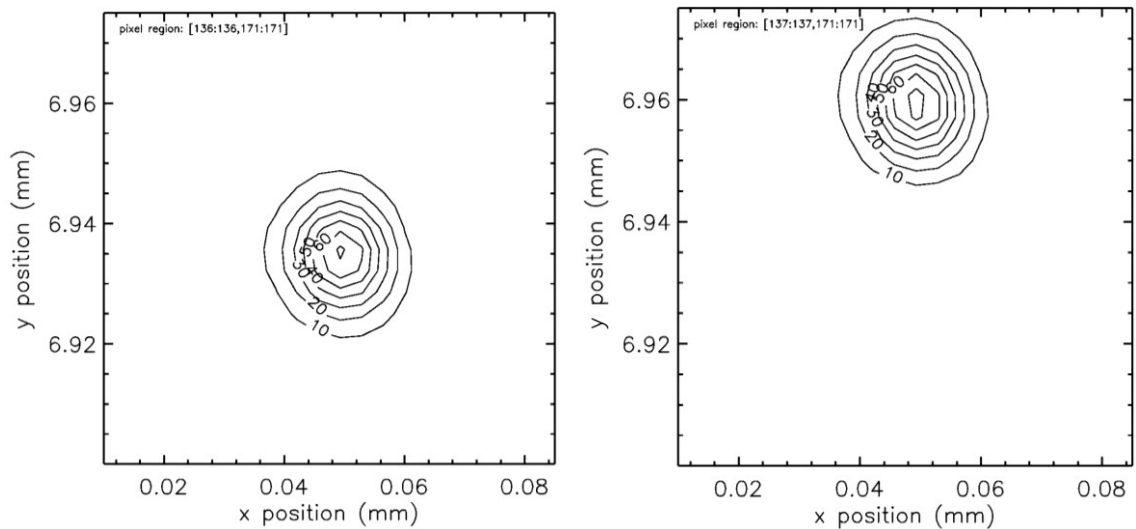


*Figure 16. IPS results from S45 from two separate pixels are shown. The centers of the pixels are in the central ring on each plot. In both cases, the FWHM is 5.2 μm, containing 3.4% of the total pixel area. The fill factor of these pixels is 4.8%.*

Since the measured PDE values in Figure 12 are very similar, it makes sense that the IPS functions should also be similar. The FWHM values range from 5.2 μm to 15.2 μm, which is not expected. Since the IPS functions are narrow in these devices, the results are significantly influenced by the laser spot size. Since the IPS function seems to be roughly the same size as the laser spot size (~5 μm), the variation results in relatively large changes in the IPS function if the laser is out of focus. We suspect that the true IPS function on each detector is close to that of S45, given their agreement in PDE values and the uncertainty in the laser spot size.

### 5.1.6 Crosstalk

Crosstalk is the correlation of events in neighboring pixels. The original testing plan required the measurement of crosstalk in an experiment identical to IPS except for the data

analysis. However, uncertainty in the laser spot size significantly affects the crosstalk data analysis. This is unavoidable in the IPS experiment, but we updated the crosstalk experiment to minimize the impact of the laser spot size on the result. Since the laser spot size is smaller than the pixel size (even when slightly out of focus), crosstalk was measured as the nearest neighbor trigger probability when the central pixel was illuminated with the laser spot focused on the center of the pixel.

The LFF devices showed very low crosstalk probabilities, with a nearest neighbor crosstalk probability of 0.70% for S47, 0.36% for S51, 0.27% for S45. The mean crosstalk probability between all three detectors was 0.44%.

In a GM-APD, there are two basic types of crosstalk. The first, the results for which are described above, implies that photo-generated electrons in one pixel migrate to a neighboring pixel. This results in the signal being spread over several pixels, but the signal can be reconstructed by adding the diffused signal. The second type is multiplying crosstalk, which is not evident in the LFF devices, but is in the HFF devices. When an avalanche occurs, photons are emitted from the avalanche and absorbed in neighboring pixels. If those neighboring pixels have not yet fired during the same gate, they may be triggered. In the case of multiplying crosstalk, the signal is duplicated, not displaced. In detectors with sufficiently high multiplying crosstalk, large blocks of pixels fire in a chain of events inside of a single gate.

For the HFF devices, multiplying crosstalk was calculated by measuring the correlation between events in a central pixel and events in nearby pixels. The key signature of multiplying crosstalk is that it introduces a correlation between the avalanche probabilities of the pixels involved. Diffusion of photo-generated electrons (a Poissonian process), on the other hand, results in zero correlation. One way, therefore, of measuring multiplying crosstalk is to calculate the conditional probability that a neighboring pixel will fire given an event in some chosen central pixel. The amount by which this probability exceeds what is expected from coincidental events is a measure of the multiplying crosstalk.

Figure 17 shows results from a HFF device, using a conditional probability matrix (i.e., how likely it is that a neighboring pixel will fire given that the reference pixel fires). The experimental data was taken in the absence of light. The background value of 4% at distant pixels is due to the coincidence of random dark counts. The nearest neighbors to the reference pixel are more likely to be triggered than the ones farther away. This behavior is seen regardless of gate time, overbias, or temperature, although there is less crosstalk overall between pixels with a lower bias voltage. This same method returned a null result (no significant crosstalk dependencies) for the LFF devices. Due to the high multiplying crosstalk probability observed for the HFF devices (and the influence it would have on other measurements), we decided to move forward with testing of the LFF devices for the evaluation of radiation damage.
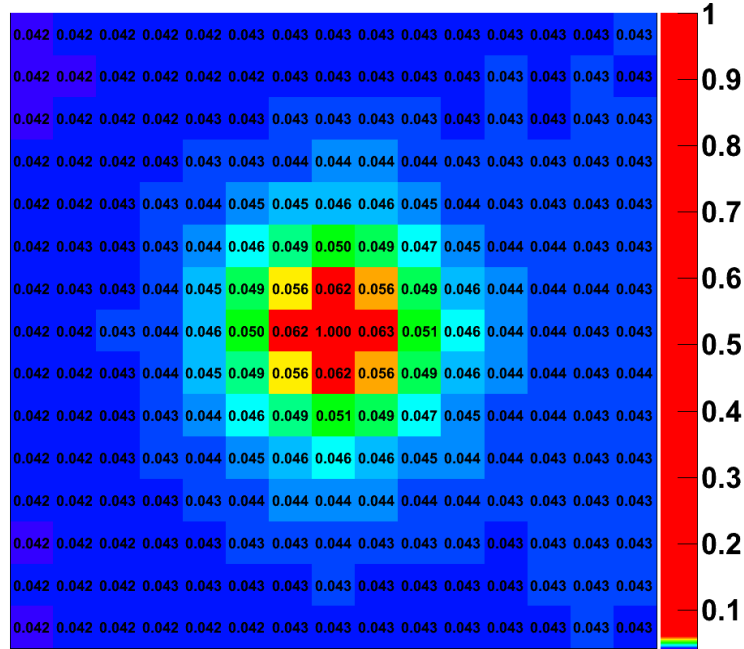
*Figure 17. This figure shows the conditional triggering probability of neighboring pixels given the triggering of the central pixel. The conditional probability is averaged over a 32 x 32 pixel grid. Nearest neighbors are triggered with a higher probability than the neighbors that are far away from the reference pixel.*

MIT Lincoln Laboratory investigated HFF device crosstalk further by measuring the dark count rate as a function of bias and temperature. It was observed that below a certain overbias threshold, the dark count rate was quite modest, in the tens of counts per second. Above the threshold, the dark count rate increased very rapidly with overbias, quickly reaching the MHz range. We theorize that this rise in DCR is due to a chain of avalanche events induced by high crosstalk probability. At higher overbias settings, where the avalanche probability due to DCR is high, the probability of crosstalk-induced events reaches a tipping point that leads to a sustained chain of events in each gate. This limits the usable range of overbias, which in turn limits the PDE. Therefore, it is important to understand the physical mechanism responsible for the precipitous rise in dark count activity with bias.

Figure 18 shows a subset of this dark data taken at 243 K for three bias values. The graph shows the probability of a pixel having fired (avalanche probability) as a function of gate time. The plotted values are based on analysis of a 5×5-pixel neighborhood, averaging over 10,000 gates. For the 29.0V bias, very few APD firings are recorded, and the observed firing rate corresponds to a DCR of about 30 Hz. As the bias increases, however, the level of firing activity rapidly increases, particularly in the early part of the gate. This is evidenced by the sharp rise in avalanche probability at shorter gate times, leading to a stable plateau. At 30.0V bias, 84% of the pixels fired in the first 2 μs. Clearly, these dark counts are not arising from a Poisson process such as thermally generated dark current.
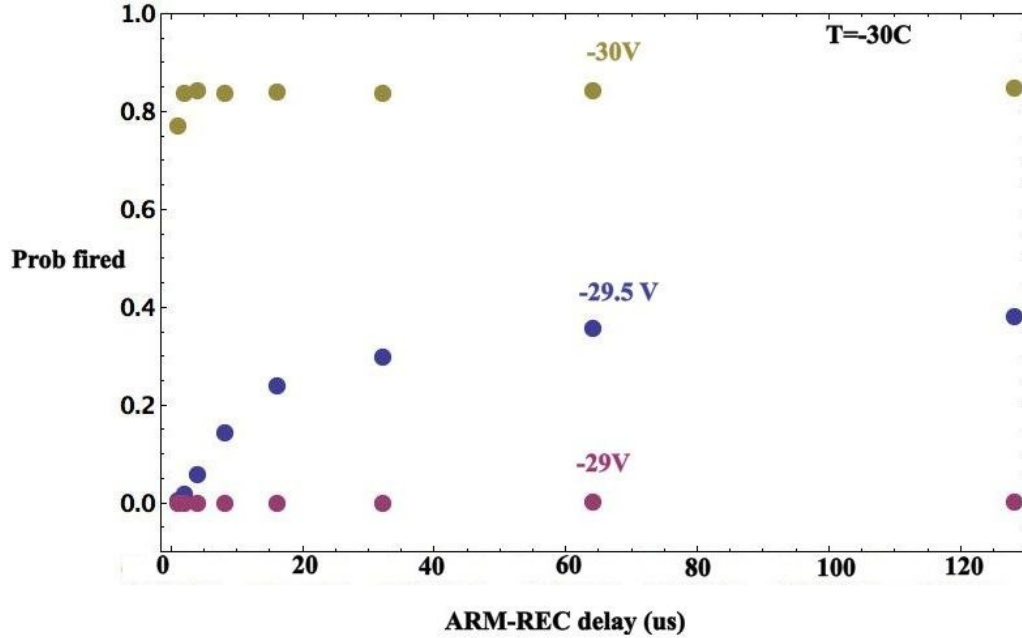
*Figure 18. This plot shows avalanche probability ("Prob fired") as a function of gate time ("ARM-REC" delay) for various bias settings. The data represents the average of a 5×5-pixel neighborhood over 10,000 frames.*

A plausible explanation for the observed behavior is crosstalk. At higher biases, the probability of crosstalk-induced events is sufficient to give rise to chains of such events. These chains cause a high level of activity early in the gate when most of the APDs are armed. After a significant fraction of the APDs has fired, those that have not are sparsely distributed and therefore have a much lower level of crosstalk. This causes the activity to subside.

In order to validate this hypothesis, a simple rate equation model was devised. In this model, the two dynamic variables are the fraction of APDs that have not yet avalanched and the density of photo- electrons created by APD light emission during an avalanche. These quantities are assumed constant over the array in space, varying only with time. When a photo-electron enters the multiplication region of an armed APD, that APD fires with some avalanche initiation probability, $\eta_d$. Upon firing, the APD generates $\eta_e$ photo-electrons in nearby pixels. Electrons are also generated by dark current. The rate at which photo-electrons are collected is described by a lifetime (which can also be a function of the fraction of APDs armed). The product $\eta_d\eta_e$ determines the severity of crosstalk.

Figure 19 compares the experimental data in Figure 18 to the best-fit results of the rate equation model described above. This comparison has also been done for cases in which the array is illuminated, and the fit is even better. This strongly confirms the hypothesis that multiplying crosstalk facilitates the rapid rise of apparent DCR when the devices are biased observed threshold. It is important to note that high crosstalk probability is not a fundamental limitation of the technology, and can be reduced with design improvements. Based on the impact of multiplying crosstalk in HFF devices, we believe that crosstalk reduction is the most important task in the future development of this technology. Crosstalk can be reduced by a number of design improvements, including microlenses, optical isolation trenches, and electrical isolation diodes between pixels. Microlenses were not included in this design because they are difficult to

21

scale to large format arrays. We believe that reducing crosstalk through pixel isolation while improving efficiency is the best way to achieve optimal device performance.
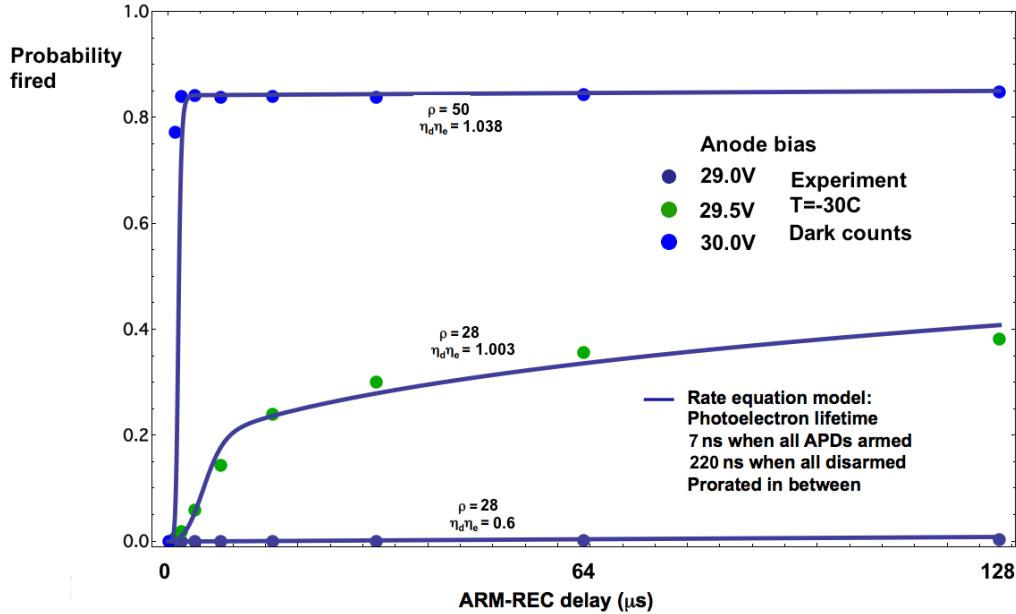


*Figure 19. This plot shows avalanche probability ("Probability fired") vs. gate time ("ARM-REC delay") for both experimental and modeled data. Note that the same carrier lifetime values are used for all three biases.*

## 5.2 Radiation Testing

The LFF devices were irradiated using the Massachusetts General Hospital's Francis H. Burr Proton Therapy Laboratory (monoenergetic 60 MeV protons). They were exposed to a cumulative dose of 50 krad (Si) in geometrically spaced doses, simulating a total of 10 solar cycles at an L2 orbit (assuming a 1 cm Al shield), where one solar cycle spans 11 years.

### 5.2.1 In-Situ Radiation Testing

The entire testing system was transported and set up at the proton beam facility so that the detectors could be tested during irradiation between doses in a vacuum- and temperature-controlled environment. The system was set up so that the detectors were in the beam path inside the dewar, with the radiation passing through a thin metal cover, which kept the dewar completely dark.

The DCR was measured between radiation doses and after the final dose. Throughout the duration of the experiment, the detectors were kept cold (~220 K). The detectors were warmed and data collection continued at room temperature for 16 hours following the final dose. Cold testing resumed when the DCR reached 99% of the settling point (calculated with an exponential decay function).

The data was collected 10,000 gates at a time, with 20 sets of 10,000 frames taken between radiation doses. The gate time was 10 μs and the hold-off time was 4.99 ms. After the final dose, the electronics suffered some failures, which were likely single-event upsets from the secondary neutron scattering. The electronics were reset and re-programmed prior to starting the final data set, leaving a small gap in the data.

Figure 20-Figure 22 show the in-situ results for the radiation testing of the devices. The data sets were kept relatively small to increase temporal resolution, which is important given the rapid decay of some of the data sets between radiation doses. All the data presented in Figure 20-Figure 22 was taken while the detectors were cold. In the plots, the median DCR of the array is taken from an exposure of 10,000 gates. 20 exposures were taken for each detector (roughly 20 minutes of wall time per detector) before each radiation dose. Data was taken overnight after the final radiation dose, totaling 360 exposures per detector of 10,000 gates each.
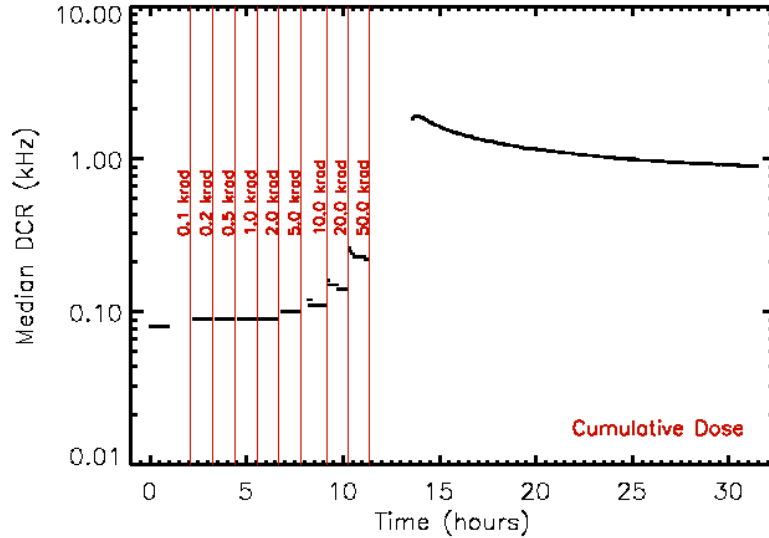


Figure 20. Median DCR vs. time over incremental radiation doses is shown for S47. Each data set has the amount of cumulative radiation noted on the vertical line immediately before it, which is marked at the time when the radiation beam stopped for that particular dose.



Figure 21. Median DCR vs. time over incremental radiation doses is shown for S51. Each data set has the amount of cumulative radiation noted on the vertical line immediately before it, which is marked at the time when the radiation beam stopped for that particular dose.

*Figure 22. Median DCR vs. time over incremental radiation doses is shown for S45. Each data set has the amount of cumulative radiation noted on the vertical line immediately before it, which is marked at the time when the radiation beam stopped for that particular dose.*
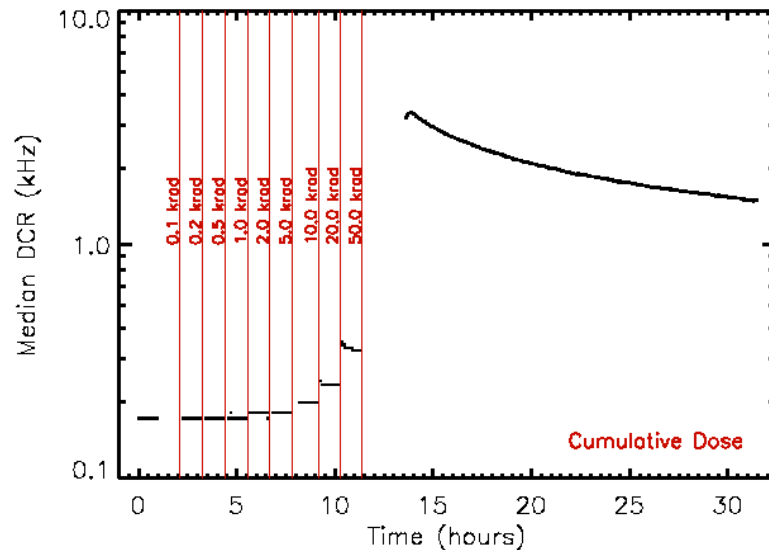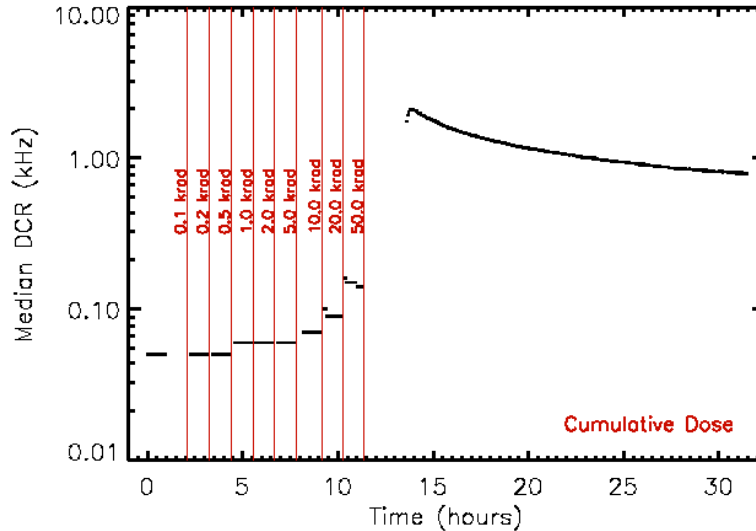
Discrete levels of DCR are evident in the data between the lower radiation doses, for which there are two reasons. The first reason is that the number of events can only be integer values because DCR is the median rather than the average, i.e. only integer values of counts are measured. The second reason is that there are a limited number of gates per exposure: the number of significant digits in the avalanche probability is a function of the number of samples. For example, the two lowest discrete DCR levels for S47 (Figure 20) are the values for DCR calculated with P=0.0008 (8 out of 10,000 gates) and for DCR calculated with P=0.0009 (9 out of 10,000 gates). With more gates per exposure, the resolution at lower DCR values would increase.

As the cumulative radiation dose increases, some exponential decay occurs in the DCR following each radiation dose. There are not enough data points to fit an exponential curve to the data between radiation doses, but the $^1/_e$ lifetime and steady-state DCR appear to increase with increasing dose. We believe that the temporary rise in DCR immediately following the radiation dose (which decays to a new steady-state value) is due to secondary radiation from the irradiated dewar and system components. At lower radiation doses, there appears to be no decay in the measured DCR. It is likely that there was a small increase, but that the increase was not significant enough to be detected. The increase in steady-state DCR is likely due to lattice damage caused by the proton radiation. Atoms that are dislodged from the lattice structure create intermediate energy states and become carrier generation sites, which increase dark current and therefore DCR. Even after an infinite amount of time, the DCR would not return to the pre-radiation steady-state value.

After the final radiation dose, the data for each detector show an exponential decay. For S47, the measured $^1/_e$ lifetime for the final data set was 5.28 hours, the measured $^1/_e$ lifetime for S51 was 6.74 hours, and the measured $^1/_e$ lifetime for S45 was 5.86 hours, or an average of 6.0 hours.

There were no detector failures during in-situ radiation testing. However, despite being behind a shield of lead bricks, the electronics suffered a single-event upset that resulted in the

failure of one readout channel on all the detectors. After resetting and power cycling the electronics, the electronics and detectors worked normally. We took the precaution of re-programming the four FPGAs in our electronics system before continuing the experiment.

### 5.2.2 Post Radiation DCR Decay

Following the cold post-radiation testing, the detectors were warmed to 300 K and brought back to the CfD along with the rest of the system. Figure 23 shows warm data, taken with the same settings as when the detector was cold.
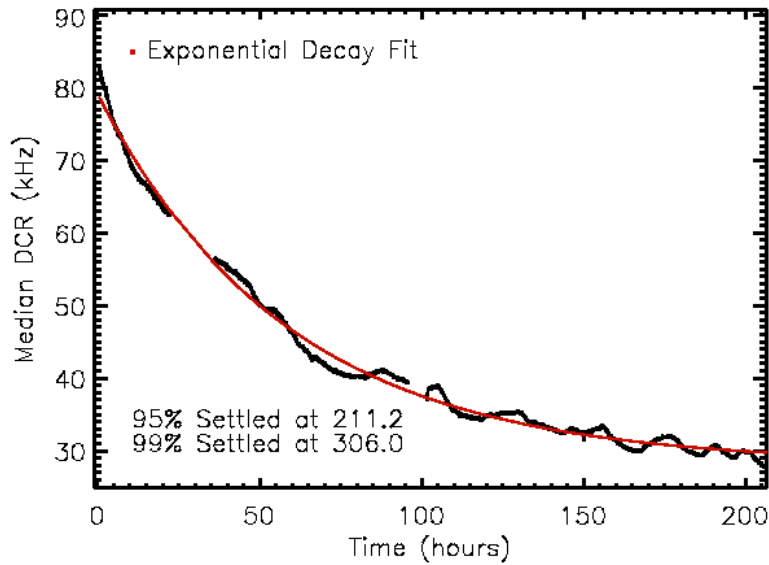


*Figure 23. This figure shows median DCR vs. time at room temperature for S45.*

Unlike the decay in in-situ radiation data, we believe that the decay at room temperature is due to annealing, or self-healing, of the lattice using energy from increased temperature – not from secondary radiation in any form. The lattice structure of a crystal represents the least amount of potential energy stored in the material. Atoms that are dislocated from the lattice will move back into position to rest in the lowest potential energy state, though that re-alignment requires energy (some dislocations require more energy than others to anneal). At room temperature, some dislodged atoms have enough energy to return to their place in the lattice structure, which removes the carrier generation sites that resulted in increased DCR. Over time, the DCR will approach a new steady-state value, which will still be higher than pre-radiation levels because some lattice damage will not anneal out at room temperature. The $^1/_e$ lifetime of the DCR decay at room temperature is ~66.5 hours.

Once the DCR had settled to the new steady-state value, the detectors were cooled and placed under vacuum. Over the course of three weeks, DCR data was taken at multiple temperatures four separate times. Figure 24shows the results from these four runs overlaid on the same plot. The mean percent standard deviation between the DCR data points at each temperature was ~1%. This consistency verified that the DCR had reached its new post-radiation steady-state level.
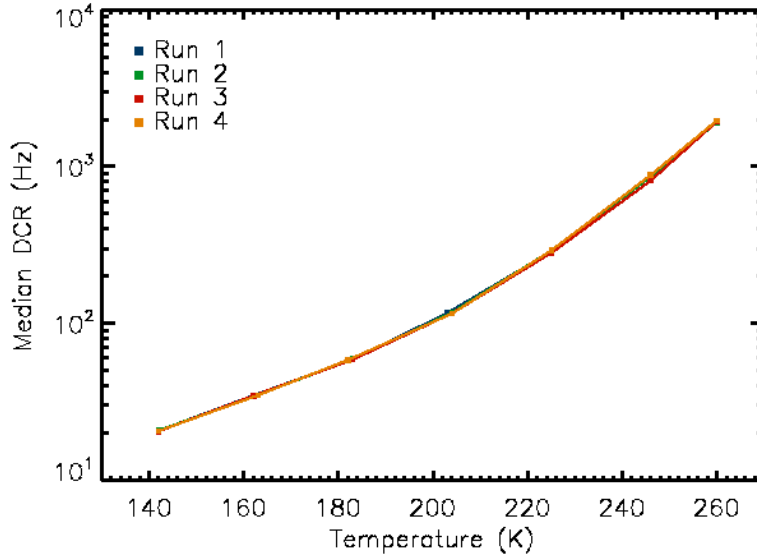
*Figure 24. This figure shows median DCR vs. temperature for S47. Each run represents a separate experiment. All four runs took place over a three week period.*

## 5.3    Post-Radiation Characterization

As discussed in section 5.2.2, the damage caused by radiation creates extra traps and dark current generation sites in the detector. We expected this damage to increase DCR and afterpulsing probability. PDE, IPS, and crosstalk are more of a function of device architecture, which should remain unaltered, and therefore we expected that these characteristics will remain unchanged from pre-radiation values. While persistent charge proved insignificant in pre-radiation testing, there was a reasonable chance that increased trap density would cause significant latency in post-radiation testing. The post-radiation testing was done with the same external bias settings as the pre-radiation data. Because the radiation damage caused the breakdown voltage of the devices to shift by +1.5 V, the results are for an effective overbias of 0.5 V. Results for an overbias of 2.0 V are also presented in section 5.3.8.

**5.3.1**   Dark Count Rate (DCR)

Post-radiation DCR was measured with the method outlined in section 5.1.1. We measured an increase in DCR at temperatures above 160 K. Additionally, the rate of increase in DCR at warmer temperatures increased to doubling roughly every 10 K instead of doubling every 17 K like the pre-radiation DCR trend. Figure 25-Figure 27 show the post-radiation testing results.
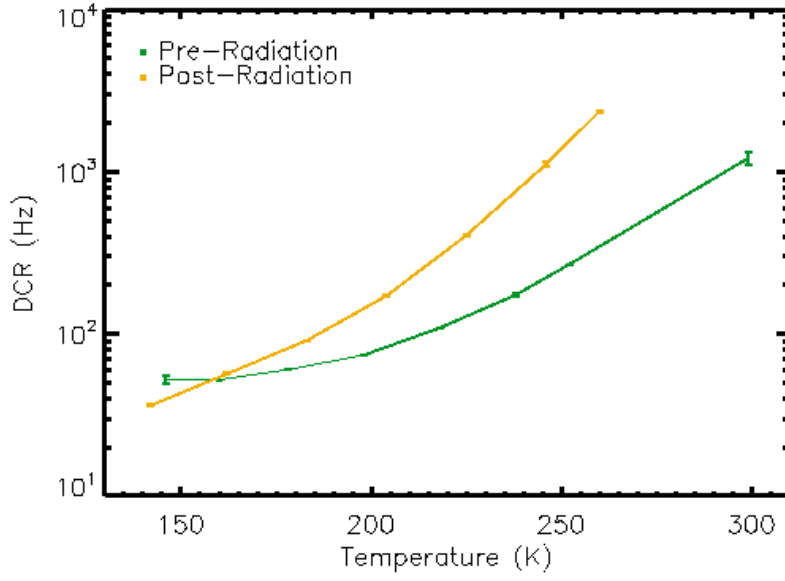
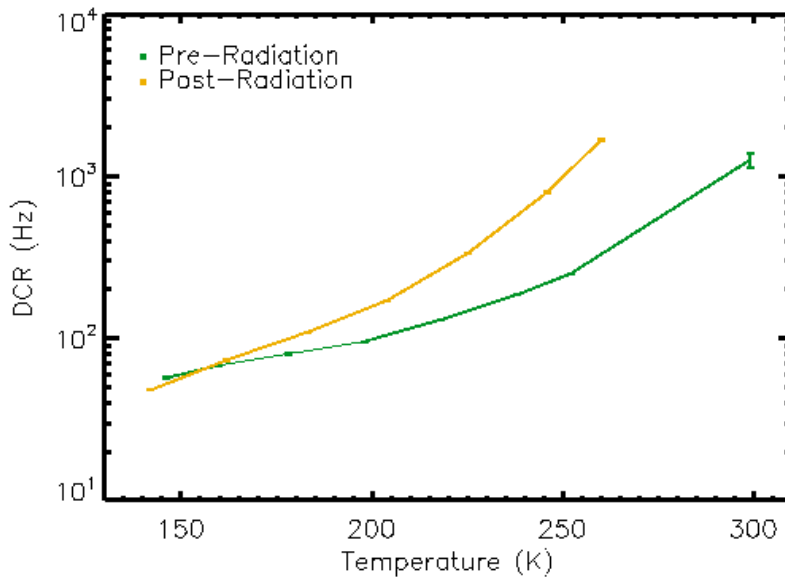*Figure 25. Median DCR vs. temperature is shown for S47.*



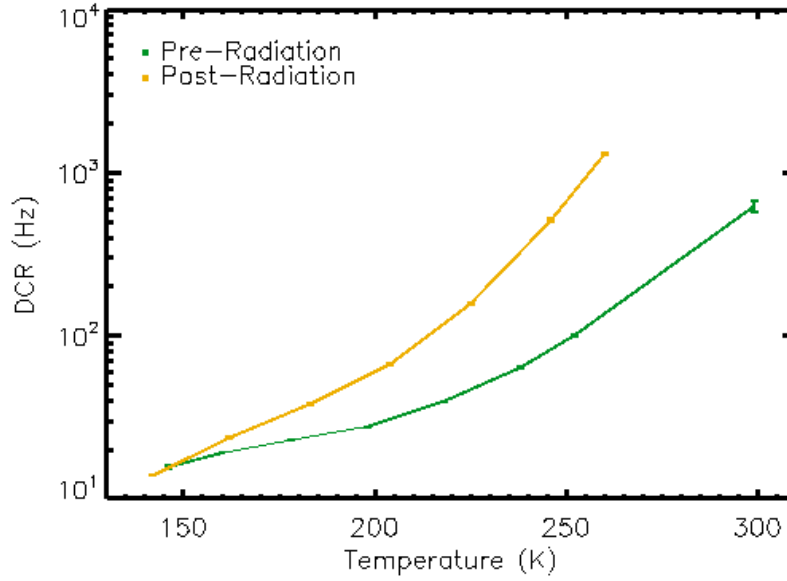*Figure 26. Median DCR vs. temperature is shown for S51.*

*Figure 27. Median DCR vs. temperature is shown for S45.*

The apparent decrease in DCR at lower temperatures may be a function of a shift in the breakdown voltage. As atoms in the silicon lattice become displaced by radiation damage, the resistivity of the bulk material increases (Li, 2002). Since the applied voltage in a GM-APD is across the entire diode structure, some of the applied voltage falls across the multiplication region, and the rest falls across the absorber region. The volume of the absorber region is much larger than that of the multiplication region, and so it sustains more radiation damage in total. With the resistance of the post-radiation absorber region now significantly increased, more of the applied voltage falls across the absorber and less falls across the multiplication region. This leads to an increase in breakdown voltage – more applied voltage is necessary to bring the electric field in the multiplication region above the critical field necessary for breakdown. However, a shift in breakdown does not explain the increase of DCR above pre-radiation levels at warmer temperatures.

CCDs and CMOS detectors experience increases in dark current after radiation damage from two main sources: bulk damage and ionization effects (Janesick, Elliot, and Pool, 1989). The latter source is caused by damage at the surface of the devices at the silicon / insulator interface. In GM-APDs, this type of damage does not affect the DCR or afterpulsing probability because the avalanche initiation probability for carriers generated at the surface of the device is effectively zero. The bulk damage is mostly comprised of deep-level defects (lattice displacement), which act as generation / recombination centers in the material. Carrier generation at deep-level defect sites is requires thermal energy, and as such is very sensitive to changes in temperature – the generated current increases exponentially with temperature. Modest cooling is often used to significantly decrease the current generated by these defects. The temperature-dependent increase in DCR is likely due to the increased generation of carriers from deep-level defects (lattice displacement). This type of carrier generation increases exponentially with increasing temperature, outpacing the effect of increased breakdown voltage.

### 5.3.2   Afterpulsing Probability

Afterpulsing probability was measured in the same way as outlined in section 5.1.2. We measured a modest increase in afterpulsing probability at all temperatures. The minimum hold-

off time required to avoid afterpulsing, which was 1 ms before irradiation, is still 1 ms for the colder temperatures, but 5 ms for the warmest temperatures. A new trend emerged that showed afterpulsing probability increases with temperatures above 200 K, though not as drastically as the increase at temperatures below 200 K. This trend is most evident in S47 (Figure 28), while S51 and S45 (Figure 29 and Figure 30) show the same trend beginning at warmer temperatures (near 220 K).
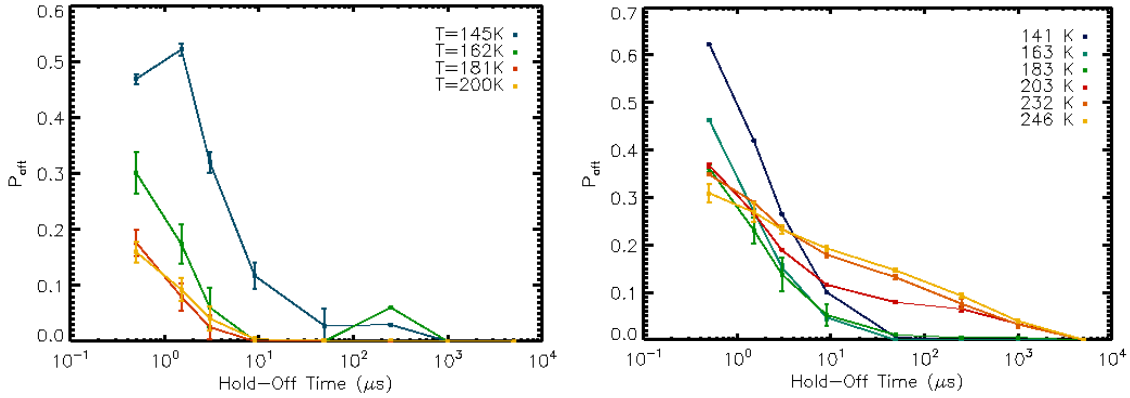


Figure 28. Median afterpulsing probability vs. arm period (hold-off time) is shown for S47 for various temperatures. The figure on the left shows pre-radiation results, and the figure on the right shows post-radiation results.



Figure 29. Median afterpulsing probability vs. arm period (hold-off time) is shown for S51 for various temperatures. The figure on the left shows pre-radiation results, and the figure on the right shows post-radiation results.

*Figure 30. Median afterpulsing probability vs. arm period (hold-off time) is shown for S45 for various temperatures. The figure on the left shows pre-radiation results, and the figure on the right shows post-radiation results.*
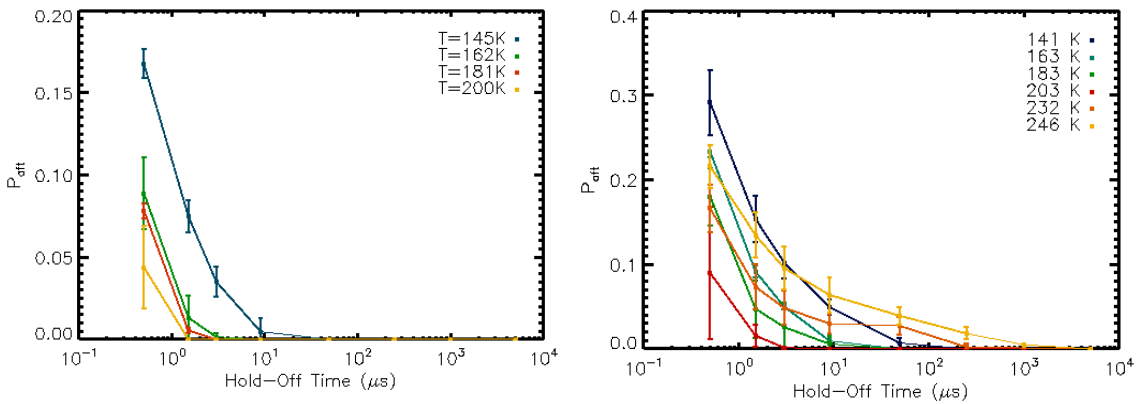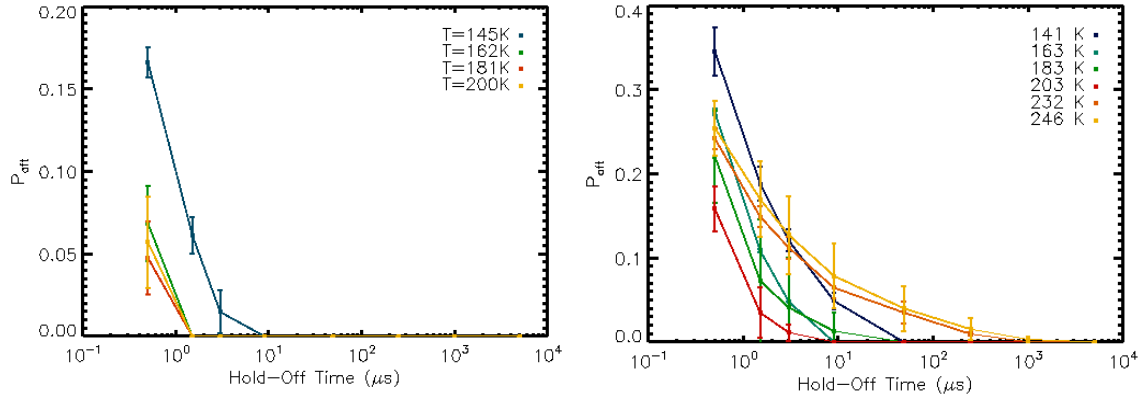
### 5.3.3 Detector Failures

At this point in the testing, two of the detectors failed due to a user error that resulted in improper biasing. Each detector is biased with a separate power supply, and the cables connecting the power supplies to the detector bias inputs were connected in a way that reversed the bias on two detectors (instead of negative voltage, two detectors received positive voltage). Because of this error, S51 and S45 were forward-biased (instead of reverse-biased) for an exposure of 100,000 gates, which lead to their permanent failure. S47 was not forward-biased, and so it was not damaged.

One explanation for the permanent failure of S45 and S51 is that the ROICs failed due to increased bias on the MOSFET gates. When reverse-biased, the diodes in each pixel are highly resistive and all of the bias voltage is dropped across the diodes. When forward-biased, the diodes are much less resistive, allowing significant current to flow, and a significant voltage is placed on the contact at the ROIC for each pixel. Since the ROIC logic operates on +3.3 V, higher voltages could have catastrophically damaged the MOSFET devices, likely by damaging the insulating layers in the gate terminals. This would permanently damage the ROICs on S51 and S45. Another theory regarding the detector failure is that the diodes were damaged by the increase in current flow, which increased their resistivity. The increase in resistance across the diodes would lead to a large increase in breakdown voltage, and the pixels would appear dead at normal bias voltages. It may be that both the diodes and the ROICs were damaged as a result of being forward-biased. Further tests have not been done because the damaged detectors now draw more current than is deemed safe for the control electronics.

This kind of failure might be avoided in future iterations of the devices by adding shunting diodes on the ROIC that divert high current away from the MOSFET devices. Another solution may be to alter the detectors' control electronics to detect an improper bias and prevent it from reaching the detectors at all. This could be done with shunting diodes as well.

Since S47 was not damaged, the results in the following sections (PDE, persistent charge, IPS, and crosstalk) are for S47 only. In pre-radiation tests, the PDE for all three detectors were within 9.3% standard deviation at peak PDE, and matched each other in low and high cut-off wavelengths. All three detectors also showed the same changes in DCR and in afterpulsing between pre- and post-radiation results. Given this consistency in behavior between the

30

detectors, we believe we can make reasonable inferences about the performance of S45 and S51 by testing S47 only.

### 5.3.4   Photon Detection Efficiency

PDE was measured the same way as in section 5.1.3. Figure 31 shows the pre- and post-radiation median PDE for S47, without correcting for fill factor. The post-radiation peak PDE is 0.18% $\pm$ 0.002% at 730 nm. This decrease is due to a decrease in effective overbias, and not the efficiency of the device. 55% of pixels were within 10% of the median and 8% were dead or hot pixels after irradiation. The short-wavelength and long-wavelength cut-offs, as well as the peak PDE wavelength, remained the same as in pre-radiation testing. Corrected for fill factor, the peak sensitivity in the center of the pixel (based on the results in section 5.3.6) was 0.7%.
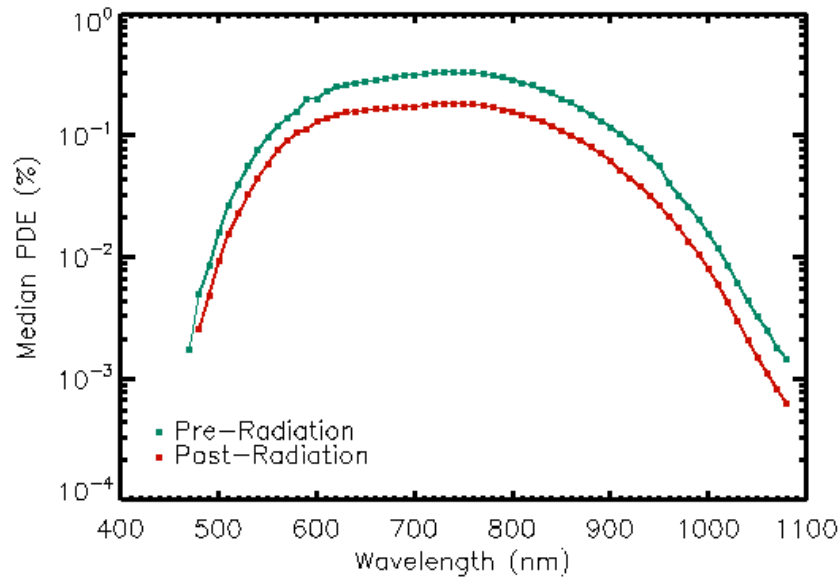


*Figure 31. Pre- and post-radiation PDE results from S47 are shown. The decrease in PDE after irradiation is due to the shift in breakdown voltage and the subsequent decrease in effective overbias.*

### 5.3.5   Persistent Charge

Persistent charge was measured the same way as in section 5.1.4. The results are shown in Figure 32. There is no evidence of persistence after irradiation at a 0.5 V overbias. This is consistent with the afterpulsing results in section 5.3.2, where there was no afterpulsing contribution measured after 1 ms of hold-off time.
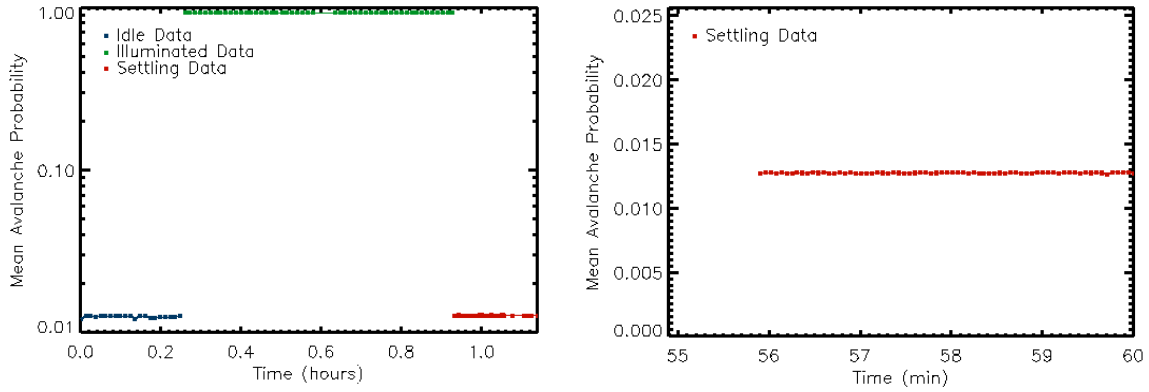
*Figure 32. Post-radiation persistent charge results for S47 are shown. Full results are shown on the left, and a close-up of the results immediately following illumination is shown on the right. There is no evidence of persistence, which is consistent with the trap lifetimes measured in section 5.3.2.*

### 5.3.6   Intra-Pixel Sensitivity (IPS)

IPS was measured the same way as in section 5.1.5. Figure 33 shows the normalized IPS function for a pixel on S47. The FWHM, correcting for laser spot size, is 12.1 μm, or 18.4% of the total area. This FWHM falls within the range of values measured in pre-radiation testing, though it is 1.9 μm larger than in pre-radiation testing (see Figure 14). We believe that no significant change in intra-pixel sensitivity has occurred due to radiation damage, given the variation between the detectors in pre-radiation testing and the uncertainty in the laser spot size.
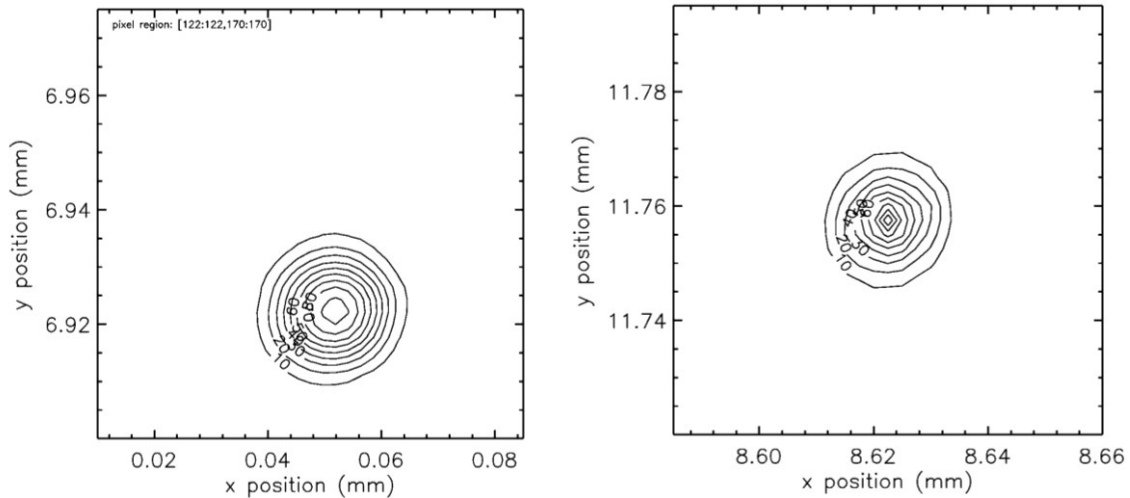


*Figure 33. IPS results from S47 are shown. The centers of the pixel are inside the central contours. The plot on the left shows pre-radiation results, and the plot on the right shows post-radiation results. The post-radiation results are corrected for laser spot size, and the FWHM is 12.1 μm, or 18.4% of the total pixel area.*

### 5.3.7   Crosstalk

Crosstalk was measured in the same way as outlined in section 5.1.6. The crosstalk probability for S47 was 0.49%, which falls within the range of pre-radiation crosstalk probabilities and is close to the pre-radiation mean of 0.44%.

**5.3.8**   Higher Overbias Testing

The post-radiation data presented above were taken at an overbias of 0.5 V. To match the testing conditions of the pre-radiation characterization, testing at 2.0 V overbias was also done. The results at an overbias of 2.0 V include DCR and persistent charge. Afterpulsing probability, PDE, and crosstalk could not be characterized due to extraordinary persistence in the device.

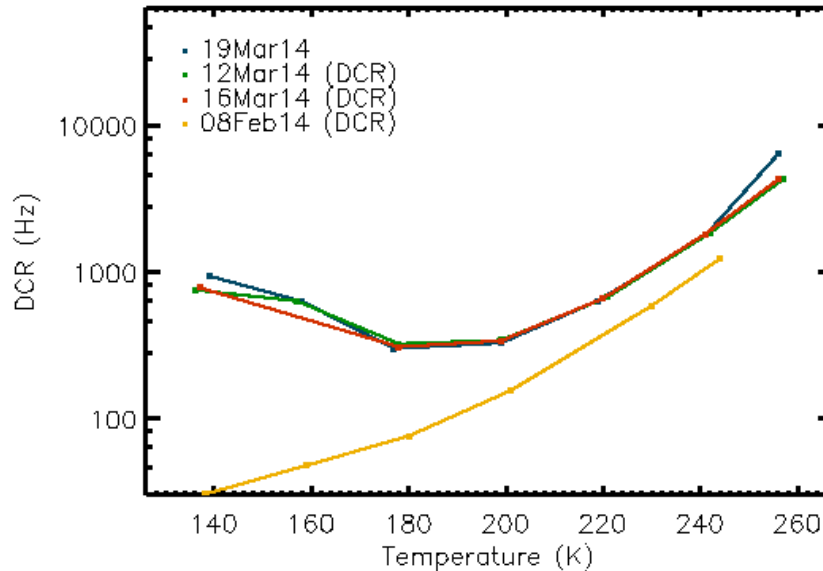Figure 34 shows post-radiation DCR results at overbiases of 0.5 V and 2.0 V.



*Figure 34. Post-radiation DCR results for S47 are shown with an overbias of 2.0 V and 0.5 V. The curves from March (blue, green, and red) were taken at a 2.0 V overbias, and the yellow curve was taken at a 0.5 V overbias, The increase in DCR for the higher overbias results at temperatures below 200 K are significantly affected by afterpulsing. The hold-off time for the 2.0 V overbias measurements was 10 ms.*

The 2.0 V overbias results are significantly affected by afterpulsing at temperatures below 200 K, even at hold-off times of 10 ms. There was no measured improvement between hold-off times of 5 ms and hold-off times of 10 ms. This result implies that the trap lifetimes of the device are much longer than 10 ms.

Measuring the afterpulsing with hold-off times longer than 1 s was not practical using the method described in section 5.1.2; a single data set at one temperature would take over 11 days. Given the length of the trap lifetimes expected at 2.0 V overbias, it was reasonable that the effects of afterpulsing could be measured in the persistent charge experiment. Figure 35 shows the persistent charge results for an overbias of 2.0 V.
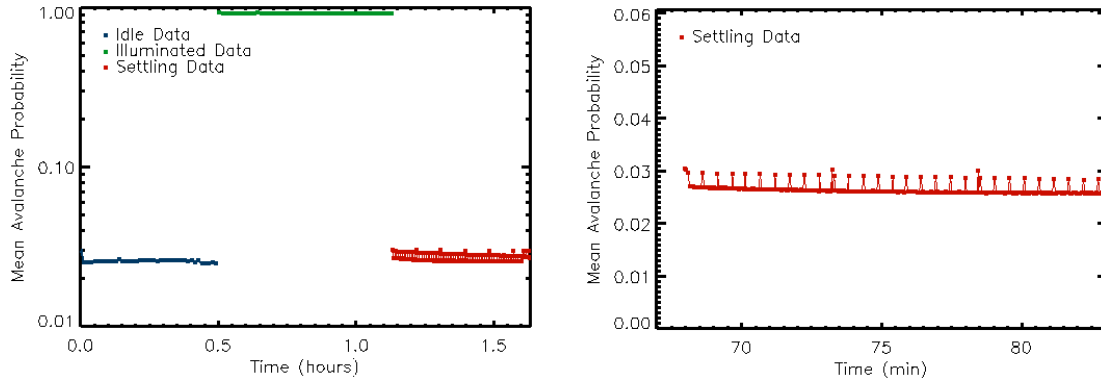
*Figure 35. Post-radiation persistent charge results for S47 are shown with an overbias of 2.0 V. The $^{1}/_{e}$ lifetime of the post-illuminated decay in the settling data is ~6 minutes.*

The persistence is significant with a $^{1}/_{e}$ lifetime of ~6 minutes. This level of persistence makes operation of the device at 2.0 V overbias impractical. Therefore, after 50 krad (Si) of radiation, the device should be operated at lower overbias settings. Post-radiation PDE results are not presented for a 2.0 V overbias because they would be unreliable due to the extraordinary persistence and the impracticality of measuring the afterpulsing probability.

# 6. Conclusions

Three of five success criteria (see section 4) were met. A HFF device was fabricated with a 256×256 format and a pixel size of 25 μm, meeting the first criterion. The second criterion was to demonstrate a PDE of at least 35% at 350 nm, 50% at 650 nm, and 15% at 1000 nm. This criterion was not met. The maximum PDE of the HFF device was ~15% near 650 nm, <1% at 1000 nm, and the device had a short-wavelength cutoff of ~450 nm. PDE will be improved in future designs by reducing crosstalk, which will allow the device to operate at higher overbiases. This will increase the avalanche initiation probability and the PDE (see Figure 9). Both the LFF and HFF devices demonstrated zero read noise, meeting the third criterion. As discussed in section 5, LFF devices were used to compare pre- and post-radiation results for the fourth criterion, though two tests (post-radiation PDE and persistent charge) could not be completed due to lack of time. The HFF devices could not be fully characterized due to crosstalk. Finally, each experiment was completed 3 times without warming the detectors, meeting the final criterion.

# 7. References

Albota MA, Heinrichs RM, Kocher DG, Fouche DG, Player BE, O'Brien ME, Aull BF, Zayhowski JJ, Mooney J, Willard BC, Carlson RR. 2002, "Three-dimensional imaging laser radar with a photon-counting avalanche photodiode array and microchip laser," Appl Opt. 2002 Dec 20;41(36):7671-8

Aull, B. F. "3D Imaging with Geiger-mode Avalanche Photodiodes," Optics and Photonics News 16, 42-46 (2005)

Aull, B., Burns J., Chen C., Felton B., Hanson H., Keast C., Knecht J., Loomis A., Renzi M., Soares A., Suntharalingam V. Warner K., Wolfson D., Yost D., Young D., "Laser radar imager based on three-dimensional integration of Geiger-mode avalanche photodiodes with

two SOI timing-circuit layers," ISSCC Dig. Tech. Papers, pp 304-305 (2006)

Cova, S., M. Ghioni, A. Lacaita, and F. Zappa, "Avalanche photodiodes and quenching circuits for single-photon detection," Applied Optics 35, 1956-1976, 1996

Daigle, O., Gach, J.-L., Guillaume, C., Lessard, S., Carignan, C., & Blais-Ouellette, S. 2008, "CCCP: a CCD controller for counting photons," SPIE, 7014, pp. 70146L-70146L-10

Daigle, O., Carignan, C., Gach, J. L., Guillaume, C., Lessard, S., Fortin, C. A., & Blais-Ouellette, S. 2009, "Extreme Faint Flux Imaging with an EMCCD," PASP, 121, 866

Daly, E. et al. 2004, "Standards for Space Radiation Environments and Effects," ESA Special Publication, 536, 175

Figer, D.F., Agronin, M., Balleza, J., Barkhouser, R., Bergeron, L., Greene, G. R., McCandliss, S. R., Rauscher, B. J., Reeves, T., Regan, M. W., Sharma, U., Stockman, H. S. 2003, "The Independent Detector Testing Laboratory and the NGST Detector Program," *SPIE*, 4850, 981

Figer, D.F., Rauscher, B. J., Regan, M. W., Morse, E., Balleza, J., Bergeron, L., & Stockman, H. S. 2004, "Independent Testing of *JWST* Detector Prototypes," *SPIE*, 5167, 270

Figer, D.F., Regan, M., Morse, E. & Balleza, J. 2005, "Independent Testing of Silicon PIN Detector Arrays for LSST," AAS, 205, 108.08

Hadwen, B. J.; Camas, M. A.; Robbins, M. S. 2004, "The Effects of Co ^60 Gamma Radiation on Electron Multiplying Charge-Coupled Devices," IEEE Transactions on Nuclear Science, vol. 51, issue 5, pp. 2747-2752

Janesick, James; Elliott, Tom; Pool, Fred. 1989, "Radiation Damage in Scientific Charge-Coupled Devices," IEEE Transactions on Nuclear Science, vol. 36, issue 1, pp. 572-578

Li, Zheng. 2002, "Radiation Hardness/Tolerance of Si Sensors/Detectors for Nuclear and High Energy Physics Experiments," Proceedings: Pixel 2002: International Workshop on Semiconductor Pixel Detectors for Particles and X-Rays, Carmel, USA, September 9-12, 2002.

Marino, R. M., T. Stephens, R. E. Hatch, J. L. McLaughlin, J. G. Mooney, M. E. O'Brien, G. S. Rowe, J. S. Adams, L. Skelly, R. C. Knowlton, S. E. Forman, & W. R. Davis 2003, "A compact 3D imaging laser radar system using Geiger-mode APD arrays: system and measurements," SPIE Vol. 5086, 1-15

Pool, P. J., Morris, D. G., Burt, D. J., Bell, R. T., Holland, A. D., & Smith, D. R. 2005, "Application of electron multiplying CCD technology in space instrumentation," Proc. of SPIE Vol. 5902, 67

Rauscher, B. J., Figer, D. F., et al. 2004, "Detectors for the James Webb Space Telescope near-infrared spectrograph," SPIE Vol. 5487, 710

Simms, L., Figer, D. F. et al. 2007, "First results with a 4Kx4K Si PIN detector," SPIE, 6619

Smith, David R., Ingley, Richard, and Holland, Andrew D. 2006, "Proton Irradiation of EMCCDs," IEEE Transactions on Electron Devices, Vol. 53, No. 2

Trauger, J.T., & Traub, W.A. 2007, "A laboratory demonstration of the capability to image an Earth-like extrasolar planet," Nature, 446, 771

Westhoff, Richard C., Michael K. Rose, James A. Gregory, Gregory D.Berthiaume, John F. Seely, Thomas N. Woods, & Gregory Ucker 2007, "Radiation-Hard, Charge-Coupled Devices for the Extreme Ultraviolet Variability Experiment," SPIE Vol. 6686

Westhoff, Richard C., Reich, Richard C., Loomis, Andrew H., & Gregory, James A. 2007, "Integrated Processes for Detector Back Illumination," Proc, 2007 International Image Sensor Workshop

Woolf, N.J., Smith, P. S. Traub, W. A. and Jucks, K. W. 2002, "The Spectrum of Earthshine: A Pale Blue Dot Observed from the Ground," ApJ, 574, 430

# 8. Team Members and Affiliations

| Name | Affiliation | Task |
|---|---|---|
| Donald F. Figer | RIT | PI - Overall responsibility |
| Brian Aull | LL | Co-I – APD design and device hybridization |
| Daniel Schuette | LL | Co-I – ROIC design and testing |
| Bob Reich | LL | Co-I – Management oversight |
| Joong Lee | RIT | Radiation testing design and execution |
| Brandon Hanold | RIT | Detector testing design and integration |
| Tom Montagliano | RIT | Data acquisition and reduction |
| Don Stauffer | RIT | Software design |
| Brian Ashe | RIT | Management |

# 9. Glossary

| | |
|---|---|
| $\overline{c}$ | counted events |
| CCD | charge coupled device |
| CMOS | complementary metal oxide semiconductor |
| CTE | charge transfer efficiency |
| e⁻ | electron |
| FITS | flexible image transport system |
| FWHM | full width at half maximum |
| HFF | high-fill-factor |
| L2 | Lagrange point #2 |
| LIDAR | LIght Detection And Ranging |
| LL | Lincoln Laboratory |
| MOSIS | Metal Oxide Semiconductor Implementation Service |
| NIEL | nonionizing energy loss |
| RIDL | Rochester Imaging Detector Laboratory |
| RIT | Rochester Institute of Technology |
| ROIC | readout integrated circuit |
| SNR | signal-to-noise ratio |
| SPACERAD | abbreviation for Space Environment and Effects Modeling Software product |
| SPENVIS | Space Environment Information System |
| SRIM | Stopping and Range of Ions in Matter |
| TID | total integrated dose |
| TRL | technology readiness level |